We are IntechOpen, the world's leading publisher of Open Access books
Built by scientists, for scientists

6,300
Open access books available

171,000
International authors and editors

190M
Downloads

Our authors are among the

154
Countries delivered to

TOP 1%
most cited scientists

12.2%
Contributors from top 500 universities

CLARIVATE ANALYTICS
BOOK CITATION INDEX
INDEXED

WEB OF SCIENCE™

Selection of our books indexed in the Book Citation Index in Web of Science™ Core Collection (BKCI)

Interested in publishing with us?
Contact book.department@intechopen.com

Numbers displayed above are based on latest data collected.
For more information visit www.intechopen.com

Chapter 1

Modeling and Analysis of Molten Pool Behavior for Submerged Arc Welding Process with Single and Multi-Wire Electrodes

Dae-Won Cho

Additional information is available at the end of the chapter

http://dx.doi.org/10.5772/intechopen.76725

Abstract

This chapter describes the procedure of modelling and analysis of molten pool behavior for submerged arc welding process with single and multi-electrodes. As submerged arc welding process is conducted under the covered flux, it is very difficult to extract the various arc shapes and its physical models such as arc heat flux, arc pressure, electromagnetic force, droplet impingement and heat source by consumed flux. This chapter suggests the way to extract the various arc models for submerged arc welding process for single and multi-wire electrodes. As the droplet movements in submerged arc welding process are different from the arc current, this chapter tries to make the flux-wall guided droplet impingement models for low current value (I < 500 A) and spray droplet impingement model for high current value. In high current single electrode submerged arc welding, the molten pool flow pattern for different electrode angle and welding signal wave forms (DC and AC) are analyzed. This chapter also modeled and analyzed the molten pool behaviors for multi-wire electrodes in submerged arc welding process with an arc interaction models for different current values.

Keywords: computational fluid dynamics (CFD), submerged arc welding (SAW), molten pool flow, arc interaction, multi-wire electrode

1. Introduction

Submerged arc welding (SAW) is a very complex process that includes physical and chemical reactions. Moreover, it is very difficult to investigate the whole SAW process using numerical simulations [1–4]. However, the molten zone and heat-affected zone (HAZ) could be estimated using the finite element method (FEM) and considering just the conduction heat transfer.

IntechOpen

© 2018 The Author(s). Licensee IntechOpen. This chapter is distributed under the terms of the Creative Commons Attribution License (http://creativecommons.org/licenses/by/3.0), which permits unrestricted use, distribution, and reproduction in any medium, provided the original work is properly cited. CC BY

Wen et al. [1] modeled multi-wire SAW of thick-wall line pipe and calculated the thermal distributions under various welding conditions. Sharma et al. [2] predicted the temperature distributions and angular distortions in single-pass butt joints using three-dimensional simulations. Mahapatra et al. [3] suggested and validated a volumetric heat source model of twin-wire SAW by using different electrode diameters and polarities. Kiran et al. [4] simulated a three-dimensional heat transfer of a V-groove tandem SAW process for various welding conditions using FEM. However, these studies with FEM only considered the heat conduction transfer in the welding process, which is insufficient to explain the curve weld bead such as fingertip penetration.

To overcome these disadvantages, computational fluid dynamics (CFD) is widely used to investigate molten pool flows and final weld beads because it makes it possible to approach the welding process more realistically [5]. Considering the importance of weld pool convection in the welding process, numerous researchers have attempted to analyze the heat transfer and fluid flow. Kim et al. [6] calculated the convective heat transfer and resultant temperature distributions for a filet gas metal arc welding (GMAW) process. Kim et al. [7] obtained the thermal data and analyzed the molten pool flows for various driving forces in stationary gas tungsten arc welding (GTAW). However, these studies assumed that the welding process was in a quasi-steady-state. Thus it was very difficult to approximate the droplet impingent and arc variation with alternating current (AC). Therefore, it is necessary to apply a transient analysis to the welding simulation because it can detect the free surface variation during the simulation time. One transient analysis method is the volume of fluid (VOF) method, which can track the molten pool surface; therefore, the variable models from arc plasma could be implemented in the simulations. Cho et al. [8] calculated the electromagnetic force (EMF) with mapping coordinates in V-groove GTAW and GMAW, and then applied it to the numerical simulation to obtain the dynamic molten pool behavior and final weld bead using the commercial software, Flow-3D. With the advantage of VOF transient simulation, Cho et al. [9] could calculate unstable molten pool flow patterns such as humping and overflow in V-groove positional GMAW. Cho et al. [10] obtained the heat flux distribution of the arc plasma in gas hollow tungsten arc welding (GHTAW) using the Abel inversion method and applied it to the VOF model to predict the molten zone area. Additionally, a more complex welding process can also be calculated by VOF. Cho and Na [11] conducted a laser welding simulation that included the multiple reflection and keyhole formation. Moreover, Cho and Na [12] conducted the three-dimensional laser-GMA hybrid welding, which adopted the laser welding and GMAW. Han et al. [13] compared the driving forces for the weld pool dynamics in GTAW and laser welding. The VOF method could also be applied to describe the alloying element distributions and pore generation in the laser-GMA hybrid welding process [14].

The modeling and the molten pool flow analysis of SAW process are mostly conducted by Cho et al. [15–21]. Cho et al. [15] conducted molten pool analysis of SAW for single electrode for high-current ($I > 500$ A) condition with spray metal transfer droplet impingement. They considered electrode angle and wave form and modeled to analyze the molten pool behavior for single electrode direct current (DC) and alternative current (AC) welding signals. It was found that the penetration of weld bead is closely related with electrode angle and waveform of welding signal. Cho et al. [16] also found that droplet impingement of low-current ($I < 500$)

http://dx.doi.org/10.5772/intechopen.76725

could be expected as a flux-wall guided (FWG) metal transfer using CFD simulation. They modeled FWG metal transfer with a moving cylinder and randomly directed droplet impingement. Therefore, it is possible to simulate how porosity can be trapped in the V-groove joint with a FWG metal transfer. For better productivity, the multi-electrode SAW process is proposed. Kiran et al. [17] developed physical and regression equations to predict the arc interaction and arc size as a function of the welding conditions for tandem submerged arc welding process. They modeled arc center displacements for tandem SAW under different welding conditions with a spring model. It was found that the arc center displacement of high current shifted less while that of low current shifted wider. Cho et al. [18] applied the arc interaction effect to simulate the molten pool behavior for tandem SAW process. They compared the various molten pool flow patterns where the combinations of the welding signals were different. Moreover, they found that the direction of droplet impingement was very important to expect the welding penetration. Kiran et al. [19] analyzed the temperature histories of tandem SAW CFD simulations within the same heat input. They compared cooling times from 800 to 500°C and volume fractions for different welding conditions and they found that molten pool behavior played an important role to decide the volume fraction and micro hardness. Cho et al. [20] analyzed the flux consumption rate for tandem SAW process where the heat inputs were the same except the combination of welding signals (current and voltage). They found that the arc interaction, droplet impingement direction and metal transfer mode (spray & FWG) affected the overall flux consumption rates. Kiran et al. [21] modeled three wire SAW molten pool simulation which considered arc center displacement and droplet impingement with a physical approach and then analyzed molten pool flow patterns. This chapter briefly introduces the contents how to model and analyze the molten pool behaviors from numerical simulations for single and multi-wire SAW process.

2. Modeling of molten pool behavior for SAW process

2.1. CFD modeling for single electrode

Figure 1 shows a schematic diagram of SAW to allow the following characteristics to be understood [15]: (a) the flux and molten slag cover the overall weld bead and, (b) the fabricated flux wall protects the flux cavity.

Although it is very difficult to observe the metal transfer of SAW, some previous studies succeeded in capturing the motion of a droplet in SAW. Franz [22] and Van Adrichem [23] observed the metal transfer through a ceramic tube using a X-ray cinematography and found that drops travel in free flight to the weld pool, or they may project sideways to collide with the molten flux wall. This metal transfer in SAW is the so-called flux-wall guided (FWG) transfer, as shown in **Figure 2**.

During the SAW process, a small portion of the flux is melted and consumed. Chandel [24] found that the flux consumption relies upon three sources: (a) conduction from the molten metal, (b) radiation from arc and (c) resistance heating of the slag. However, their individual

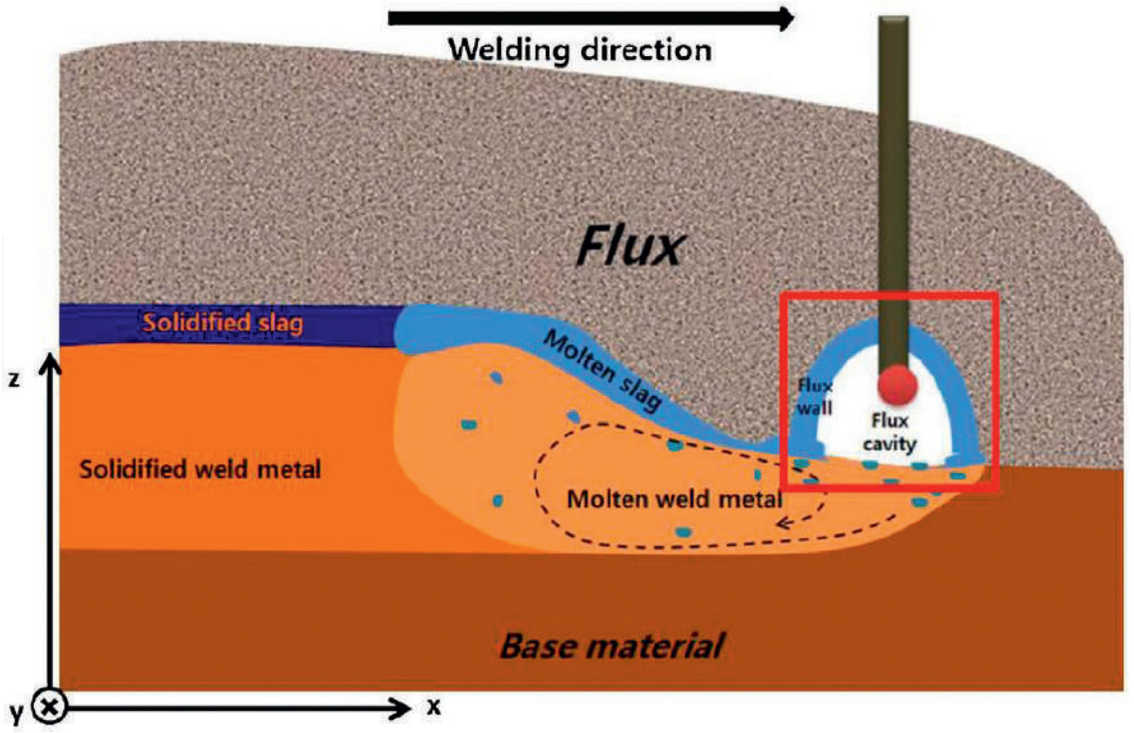

Figure 1. Schematic of SAW [15].

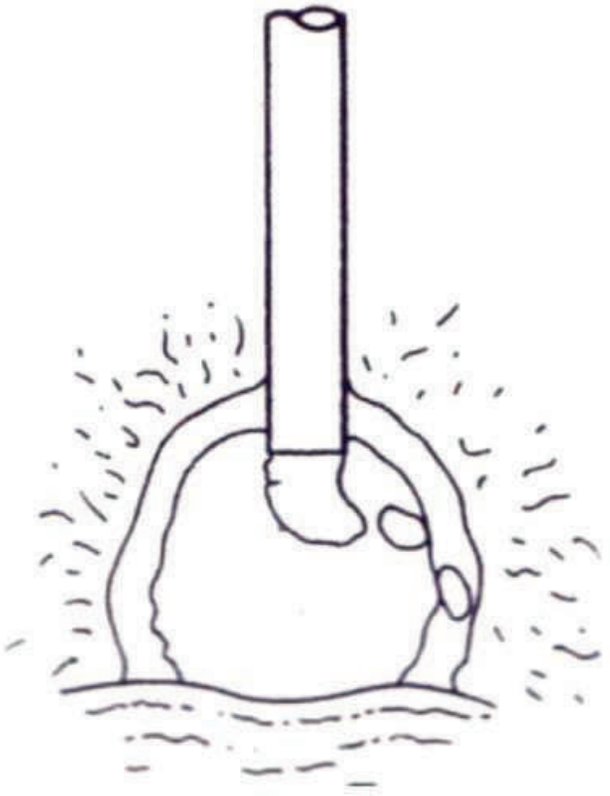

Figure 2. FWG transfer in SAW [15].

http://dx.doi.org/10.5772/intechopen.76725

contributions to flux consumption are still unclear. In any case, the total flux consumption can be calculated by measuring the mass of the flux used. Renwick and Patchett [25] analyzed the relations between welding parameters and the flux consumption and found that flux consumption initially increased with increasing current, reached a maximum, and then decreased. Chandel [24] also measured the flux consumption of SAW with various welding parameters and showed that the flux consumption reached a peak value at 500 A and decreased at higher currents, as shown in **Figure 3** [15]. This decrease at a high current is a result of the increasing current causing the droplet size to decrease. Therefore, the contact area between the droplet and the flux-wall could be decreased, as shown in **Figure 4**. In short, FWG transfer is difficult to observe at high current and the spray mode of transfer can be expected to be considered in high current SAW [15].

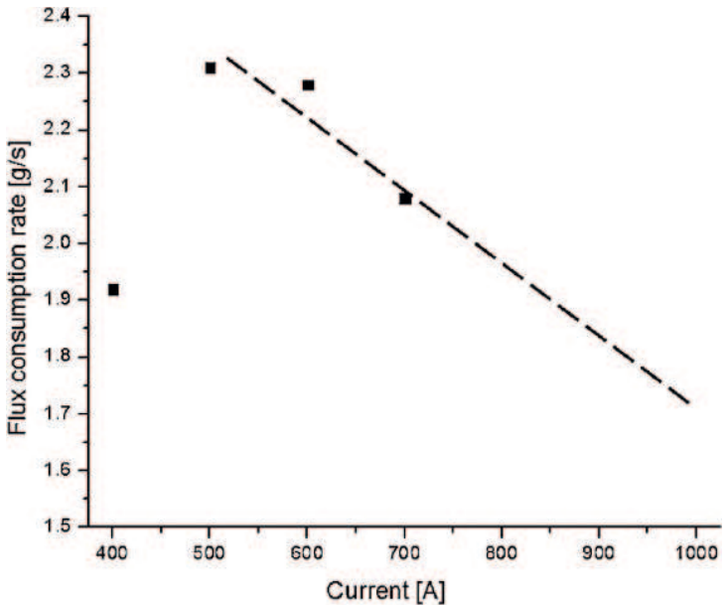

Figure 3. Current vs. flux consumption rate in single DC [15].

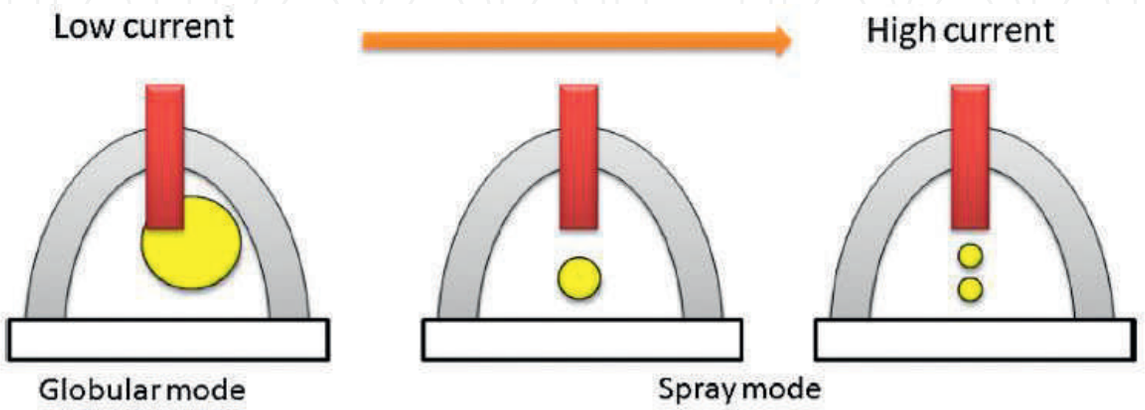

Figure 4. Expected metal transfer in single SAW process [15].

2.1.1. Governing equations

The governing equations in the CFD simulation of a weld pool involve the mass conservation equation, momentum conservation equation (Navier-Stokes equations), and energy conservation equation. The time step used in the numerical simulation is 0.00001 s. To describe the molten pool behavior, the commercial package, Flow-3D was widely used [15, 16, 18, 21] (**Table 1**).

- Momentum equation

$$\frac{\partial \vec{V}}{\partial t} + \vec{V} \cdot \nabla \vec{V} = -\frac{\nabla p}{\rho} + \nu \nabla^2 \vec{V} + \frac{\dot{m}_s}{\rho}\left(\vec{V}_s - \vec{V}\right) + f_b \tag{1}$$

- Mass conservation equation

$$\nabla \cdot \vec{V} = \frac{\dot{m}_s}{\rho} \tag{2}$$

- Energy equation

$$\frac{\partial h}{\partial t} + \vec{V} \cdot \nabla h = \frac{1}{\rho} \nabla \cdot (k \nabla T) + \dot{h}_s, \tag{3}$$

where

$$\begin{aligned} h &= \rho_s C_s T && (T \le T_s) \\ h &= h(T_s) + h_{sl} \frac{T - T_s}{T_l - T_s} && (T_s < T \le T_l) \\ h &= h(T_l) + \rho_l C_l (T - T_l) && (T_s < T \le T_l) \end{aligned} \tag{4}$$

- VOF equation

$$\frac{\partial F}{\partial t} + \nabla \cdot \left(\vec{V} F\right) = \dot{F}_s \tag{5}$$

2.1.2. Boundary conditions

There is no heat loss from the radiation, convection and evaporation on the molten pool surface because slag and flux cover the overall weld bead as shown in **Figure 1**. In SAW, the heat is input from the slag to the molten pool and lost from the molten pool to the slag. However, the summation of the heat input and heat loss can be regarded as the slag heat transfer (q_s), and the energy boundary condition in equation (6) is used [15, 16, 18, 21].

$$k \frac{\partial T}{\partial \vec{n}} = q_a + q_{slag\_input} - q_{slag\_loss} = q_a + q_s. \tag{6}$$

Symbol	Nomenclature	Symbol	Nomenclature
ρ	Density, (solid:7.8, liquid:6.9, g/cm3)	p_A	Arc pressure
$\vec{V}$	Velocity vector	R_c	Radius of the surface curvature
ν	Kinematic viscosity	γ	Surface tension
$\dot{m}_s$	Mass source of droplet	r_w	Radius of wire, 2.0 mm
h	Enthalpy	r_d	Radius of droplet, 2.1 mm
$\dot{h}_s$	Enthalpy source of droplet	WFR	Wire feed rate
$\vec{V}_s$	Velocity vector for mass source	C_s	Specific heat of liquid, 7.32x 10^6 erg/g s K
f_b	Body force	C_p	Specific heat
h_s	Enthalpy of solid	T_o	Room temperature, 298 K
h_{sl}	Enthalpy between solid and solid	η_s	Slag efficiency of SAW
T_s	Solidus temperature, 1768 K	η_d	Droplet efficiency of SAW
T_l	Liquidus temperature, 1798 K	$\dot{m}_f$	Flux consumption (g/s)
F	Fraction of fluid	x_0, y_0	Location of the electrode center in x and y directions
$\dot{F}_s$	Volume source of droplet	x_1, y_1	Location of the arc center in x and y directions
k	Thermal conductivity	J_0	First kind of Bessel function of zero order
$\vec{n}$	Normal vector to free surface	μ_0	Permeability of vacuum, 1.26 $\times$ 10^6 H/m
q_a	Heat input from arc plasma	μ_m	Material permeability, 1.26 $\times$ 10^6 H/m
q_d	Heat input from droplet	J_z	Vertical component of the current density
q_{slag_input}	Heat transfer from slag to molten pool	J_r	Radial component of the current density
q_{slag_loss}	Heat transfer from slag to molten pool	B_θ	Angular component of the magnetic field
η_a	Arc efficiency of SAW	σ_x, σ_y	Effective radius of the arc in x-direction and y-direction
I	Current	Γ_s	Surface excess at saturation
V	Voltage	$\overline{R}$	Universal gas constant
F_b	Buoyancy force	k_1	Constant related to the entropy of segregation
γ_m^0	Surface tension of pure metal at melting point	a_1	Weight percent of sulfur
A	Negative surface tension gradient for pure metal	I_L, I_T	Current of leading and trailing electrodes
ΔH^0	Standard heat of adsorption	l_L, l_T	Arc length of leading and trailing leading electrodes
X_L, X_T	Arc center position of x-direction for leading and trailing electrodes	β_n^{ij}	Coefficients of effective radius model
$B_{\theta L}, B_{\theta T}$	Angular component of the magnetic field for leading and trailing electrodes	d	Distance between leading and trailing electrode
σ_{RL}, σ_{FL}	Rear and front effective radii of leading arc in x-direction	J_{zL}, J_{zT}	Vertical component of the current density for leading and trailing arcs

Symbol	Nomenclature	Symbol	Nomenclature
σ_{RT}, σ_{FT}	Rear and front effective radii of trailing arc in x-direction	J_{rL}, J_{rT}	Radial component of the current density for leading and trailing arcs
q_{aL}, q_{aT}	Arc heat flux for leading and trailing electrodes	P_{aL}, P_{aT}	Arc heat flux for leading and trailing electrodes

Table 1. Properties and constants used in simulations.

Previous studies found that the thermal efficiency of SAW is between 0.90 and 0.99, and many studies have used a thermal efficiency of 0.95 in numerical simulations [15, 16, 18, 21]. It is reasonable to use total thermal efficiency of 0.95 with the heat transfer from the arc plasma, droplets, and molten slag to the weld pool [15, 16, 18, 21].

$$\eta_a = \frac{q_a + q_d + q_s}{VI} \approx 0.95 \tag{7}$$

The pressure boundary on the free surface is applied as follows:

$$p = p_A + \frac{\gamma}{R_c}. \tag{8}$$

- Droplet model

The droplet efficiency relies on the wire feed rate and it is possible to be calculated using Eqs. (9) to (11). The droplet efficiency can be varied from the wire feed rate and welding signals [15, 16, 18, 21].

$$f_d = \frac{3r_w^2 WFR}{4r_d^3} \tag{9}$$

$$q_d = \frac{4}{3}\pi r_d^3 \rho [C_s(T_s - T_o) + C_l(T_d - T_s) + h_{sl}] f_d, \tag{10}$$

$$\eta_d = \frac{q_d}{VI}. \tag{11}$$

For the high current (I > 500 A), some studies proved that spray mode of metal transfer, which is very similar to droplet impingement of GMAW, can be considered as a droplet impingement model [15, 18]. However, the metal transfer of the low current (I < 500 A) can be assumed as FWG metal transfer as shown in **Figure 5** [16].

- Slag heat source model

Cho et al. [15, 16, 18]. used a slag heat source model that considers the flux consumption rate, and they assumed that the distribution of the slag heat input to the material surface would be an elliptical ring as shown in **Figure 6**. The slag heat source model can be calculated from equation (12) to (14).

http://dx.doi.org/10.5772/intechopen.76725

$$\eta_s = \frac{\dot{m}_f C_{pf}\left(T_{m,flux} - T_0\right)}{VI} \tag{12}$$

$$r_e = \sqrt{(x - x_0)^2 \left(\frac{\sigma_y}{\sigma_x}\right)^2 + (y - y_0)^2} \tag{13}$$

$$\begin{aligned} &if\ R_a < r_e \leq R_b\ \text{then,} \\ &q_s = \frac{\eta_s VI}{\pi\left(R_b^2 - R_a^2\right)}, \text{where } R_a = 3\sigma_q, R_b = R_a + 3.0mm \end{aligned} \tag{14}$$

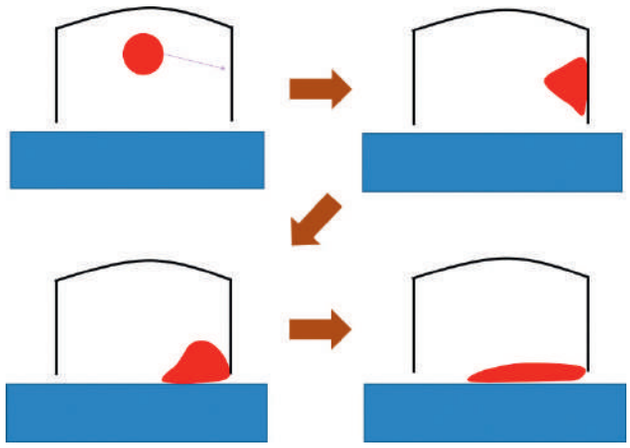

Figure 5. Schematic of droplet impingement on the wall to describe FWG transfer [16].

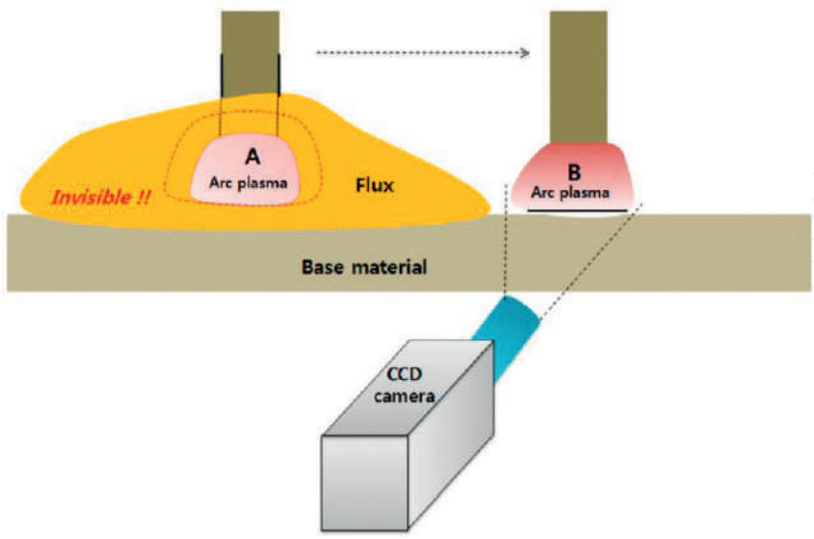

Figure 6. Process acquiring the arc plasma image [15].

- Arc heat source model

The actual arc plasma shape of SAW is very difficult to determine. Therefore, several studies assume some conditions to obtain the arc heat flux distributions [15].

a. The shape of the arc plasma inside the flux (A) is very similar to the arc plasma outside the flux (B) that just escaped (within 50 ms) as shown in **Figure 6**.

b. The metal vapor in the arc plasma root is neglected.

Therefore, it is reasonable to apply the elliptically symmetric Gaussian arc heat flux model in Eq. (15).

$$q_A(x,y) = \eta_A \frac{VI}{2\pi\sigma_x\sigma_y} \exp\left(-\frac{(x-x_1)^2}{2\sigma_x^2} - \frac{(y-y_1)^2}{2\sigma_y^2}\right) \tag{15}$$

- Arc pressure model

Due to the physical relationship, the effective radii of the arc heat flux and arc pressure are the same each other [10]. The resultant arc pressure model can be described in Eq. (16).

$$P_A(x,y) = \frac{\mu I^2}{4\pi^2\sigma_x\sigma_y} \exp\left(-\frac{(x-x_1)^2}{2\sigma_x^2} - \frac{(y-y_1)^2}{2\sigma_y^2}\right) \tag{16}$$

2.1.3. Electromagnetic force

In the arc welding process, Kou and Sun [26] found that the current density and self-induced magnetic field should be used to calculate the EMF in the molten pool. In the molten slag of a high current SAW process, however, Cho et al. [15, 16, 18] ignored the current flow effect in the molten slag because the magnitude of the current in the molten slag is tiny compared to the total current. Therefore, due to the physical relationship, the effective radius of electromagnetic force (EMF) model could be the same with that of the arc pressure and arc heat flux models [10]. For the elliptically symmetric distribution, EMF model can be calculated as follows:

$$k_1 = \frac{\sigma_y}{\sigma_x}, \quad (x-x_1)^2 + \frac{(y-y_1)^2}{k_1^2} = r_a^2 \tag{17}$$

$$J_z = \frac{I}{2\pi}\int_0^\infty \lambda J_0(\lambda r_a)\exp\left(-\lambda^2\sigma_r^2/4d_a\right)\frac{\sinh\left[\lambda(c-z)\right]}{\sinh\left(\lambda c\right)}d\lambda \tag{18}$$

$$J_r = \frac{I}{2\pi}\int_0^\infty \lambda J_1(\lambda r_a)\exp\left(-\lambda^2\sigma_r^2/4d\right)\frac{\cosh\left[\lambda(c-z)\right]}{\sinh\left(\lambda c\right)}d\lambda \tag{19}$$

$$B_\theta = \frac{\mu_m I}{2\pi}\int_0^\infty J_1(\lambda r_a)\exp\left(-\lambda^2\sigma_a^2/4d\right)\frac{\sinh\left[\lambda(c-z)\right]}{\sinh\left(\lambda c\right)}d\lambda \tag{20}$$

http://dx.doi.org/10.5772/intechopen.76725

$$F_x = -J_z B_\theta \frac{x}{r_a} \tag{21}$$

$$F_y = -J_z B_\theta \frac{y}{r_a} \tag{22}$$

$$F_z = J_z B_\theta. \tag{23}$$

2.1.4. Other models

The surface tension and buoyance force models are not affected by the arc plasma distribution [14]. The buoyancy force can be modeled by the Boussinesq approximation and then expressed in Eq. (24).

$$F_b = \rho g \beta (T - T_0) \tag{24}$$

A surface tension model that Sahoo et al. [27] developed for a binary Fe–S system is used to model the Marangoni flow. Thus, the surface tension can be expressed in Eq. (25)

$$\gamma(T) = \gamma_m^0 - A(T - T_m) - \overline{R}T\Gamma_s \ln\left(1 + k_1 a_i e^{-\Delta H^o/\overline{R}T}\right) \tag{25}$$

2.2. CFD modeling for multi-wire electrodes

For the better productivity, many industries applied two-wire or multi-electrode tandem SAW process. When the multi-wire electrodes are used, the arc shapes and the arc center positions are changed due to electromagnetic forces of arc plasma as shown in **Figure 7**.

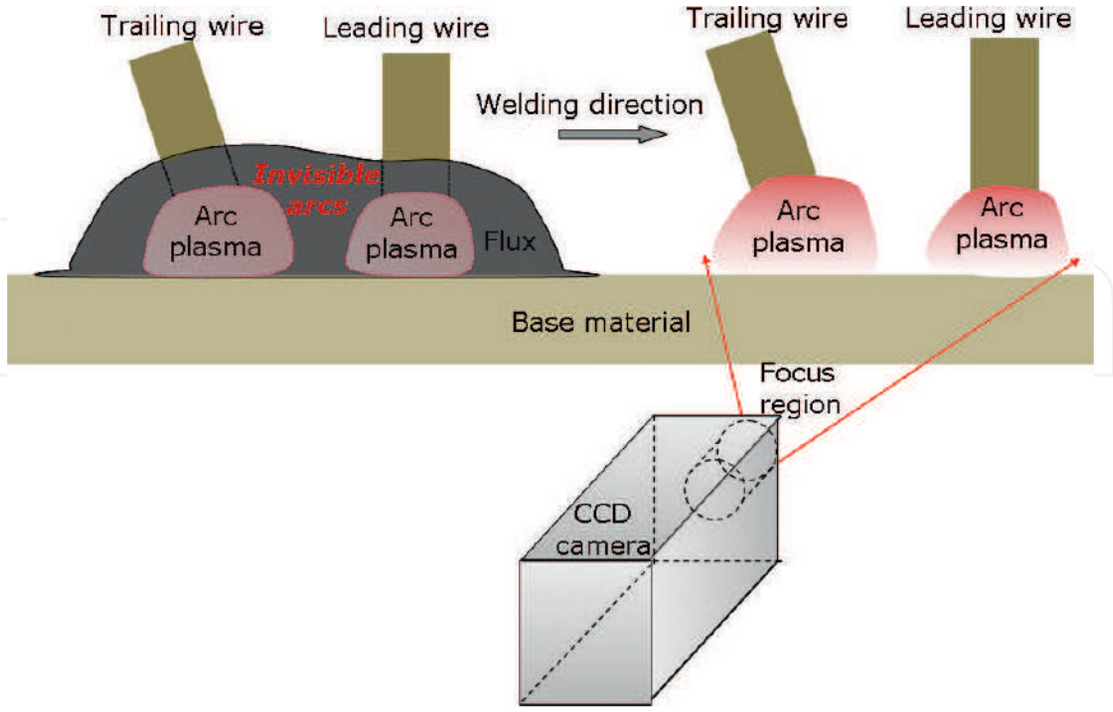

Figure 7. Schematic representation of the arc images acquisition method [17].

$$X_L = C_1\left(\frac{I_T}{I_L}\right)\left(\frac{l_L^2}{d}\right) \tag{26}$$

$$X_T = C_2\left(\frac{I_L}{I_T}\right)\left(\frac{l_T^2}{d}\right) \tag{27}$$

$$\sigma_{ij} = \beta_0^{ij} + \beta_1^{ij}I_j + \beta_2^{ij}V_j + \beta_3^{ij}X_j + \beta_4^{ij}I_j^2 + \beta_5^{ij}V_j^2 + \beta_6^{ij}X_j^2 + \beta_7^{ij}I_jV_j + \beta_8^{ij}V_jX_j + \beta_9^{ij}I_jX_j \tag{28}$$

2.2.1. Arc interaction model

Figure 7 illustrates the procedure followed to capture the arc images. The procedure to capture the arc images of multi-wire SAW process are very similar to single wire SAW process. Initially, the leading and trailing arcs are completely submerged under the granular flux, and a CCD camera starts to record side images of the arcs at a sampling rate of 1 kHz from the instant both the arcs come out of the flux. Kiran et al. [17, 21] considered the physical models for the arc center displacement and arc shape factors in two-wire and three wire tandem SAW process. From Eqs. (26) and (27), it is possible to expect that the higher current arc plasma is more stable than the lower current arc plasma. Additionally, the lower current arc plasma can be shifted more due to the arc interaction effect with AC welding signal. Kiran et al. [17] also proposed the effective radius of arc plasma model (27), where the welding current and voltage values are used.

2.2.2. Boundary conditions

The boundary conditions of single wire SAW from equation (6) to (8) are the same with that of multi-wire SAW process. However, two arc plasmas were used in the simulation so the arc heat source models, arc pressure, EMF models are different from those of the single wire model.

- Arc heat source model

As two arc plasmas were used in the simulations, two Gaussian asymmetric arc heat sources model, which contains different temperature distributions for the front and rear part in Eqs. (29) and (30). Therefore, Cho et al. [18] adopted the resultant effective radius to describe the Gaussian asymmetric arc models with DC and AC welding signals.

$$\begin{aligned} &\textit{if } \mathrm{x} \le \mathrm{x}_0 \text{ then, } q_{aL}(x,y) = \frac{\eta_a V_L I_L}{2\pi\sigma_{AL}^2}\exp\left(-\frac{(x-x_0)^2}{2\sigma_{RL}^2} - \frac{y^2}{2\sigma_{AL}^2}\right) \\ &\textit{if } \mathrm{x} > \mathrm{x}_0 \text{ then, } q_{aL}(x,y) = \frac{\eta_a V_L I_L}{2\pi\sigma_{AL}^2}\exp\left(-\frac{(x-x_0)^2}{2\sigma_{FL}^2} - \frac{y^2}{2\sigma_{AL}^2}\right) \end{aligned} \tag{29}$$

$$\begin{aligned} &\textit{if } \mathrm{x} \le \mathrm{x}_1 \text{ then, } q_{aT}(x,y) = \frac{\eta_a V_T I_T}{2\pi\sigma_{AT}^2}\exp\left(-\frac{(x-x_0)^2}{2\sigma_{RT}^2} - \frac{y^2}{2\sigma_{AT}^2}\right) \\ &\textit{if } \mathrm{x} > \mathrm{x}_1 \text{ then, } q_{aT}(x,y) = \frac{\eta_a V_T I_T}{2\pi\sigma_{AT}^2}\exp\left(-\frac{(x-x_0)^2}{2\sigma_{FT}^2} - \frac{y^2}{2\sigma_{AT}^2}\right) \end{aligned} \tag{30}$$

- Arc pressure model

The distribution of arc pressure model is the same with that of arc heat source model [10]; therefore, arc pressure model can be derived in equation (31) and (32).

$$\begin{aligned} &\textit{if } \mathrm{x} \le \mathrm{x}_0 \text{ then, } P_{aL}(x,y) = \frac{\mu_0 I_L^2}{4\pi^2 \sigma_{AL}^2} \exp\left(-\frac{(x-x_0)^2}{2\sigma_{RL}^2} - \frac{y^2}{2\sigma_{AL}^2}\right) \\ &\textit{if } \mathrm{x} > \mathrm{x}_0 \text{ then, } P_{aL}(x,y) = \frac{\mu_0 I_L^2}{4\pi^2 \sigma_{AL}^2} \exp\left(-\frac{(x-x_0)^2}{2\sigma_{FL}^2} - \frac{y^2}{2\sigma_{AL}^2}\right) \end{aligned} \tag{31}$$

$$\begin{aligned} &\textit{if } \mathrm{x} \le \mathrm{x}_1 \text{ then, } P_{aT}(x,y) = \frac{\mu_0 I_T^2}{4\pi^2 \sigma_{AT}^2} \exp\left(-\frac{(x-x_0)^2}{2\sigma_{RT}^2} - \frac{y^2}{2\sigma_{AT}^2}\right) \\ &\textit{if } \mathrm{x} > \mathrm{x}_1 \text{ then, } P_{aT}(x,y) = \frac{\mu_0 I_T^2}{4\pi^2 \sigma_{AT}^2} \exp\left(-\frac{(x-x_0)^2}{2\sigma_{FT}^2} - \frac{y^2}{2\sigma_{AT}^2}\right) \end{aligned} \tag{32}$$

- Slag heat source model

Slag heat source model in the two-wire SAW process are the same as that of single wire SAW process.

- Droplet model

Kiran et al. [17] found that the molten droplet is directed to the arc center when it is just detached. Moreover, the direction of the droplet could not be changed during the free flight. Cho et al. [18] consider that physical phenomena and then applied to the numerical simulation as shown in **Figures 8** and **9**.

The droplet efficiency relies on the wire feed rate and it is possible to be calculated using equation (9) to (11). The droplet efficiency can be varied from the wire feed rate and welding signals [15, 16, 18, 21].

2.2.3. EMF model

EMF can be induced from the two different arc plasmas; therefore EMF model used in the two-wire SAW process can be followed [18]:

$$J_{zL} = \frac{I}{2\pi} \int_0^\infty \lambda J_0(\lambda r_a) \exp\left(-\lambda^2 \sigma_{AL}^2 / 4 d_a\right) \frac{\sinh\left[\lambda(c-z)\right]}{\sinh\left(\lambda c\right)} d\lambda \tag{33}$$

$$J_{rL} = \frac{I}{2\pi} \int_0^\infty \lambda J_1(\lambda r_a) \exp\left(-\lambda^2 \sigma_{AL}^2 / 4 d_a\right) \frac{\cosh\left[\lambda(c-z)\right]}{\sinh\left(\lambda c\right)} d\lambda \tag{34}$$

$$B_{\theta L} = \frac{\mu_m I_L}{2\pi} \int_0^\infty J_1(\lambda r_a) \exp\left(-\lambda^2 \sigma_{AL}^2 / 4 d_a\right) \frac{\sinh\left[\lambda(c-z)\right]}{\sinh\left(\lambda c\right)} d\lambda \tag{35}$$

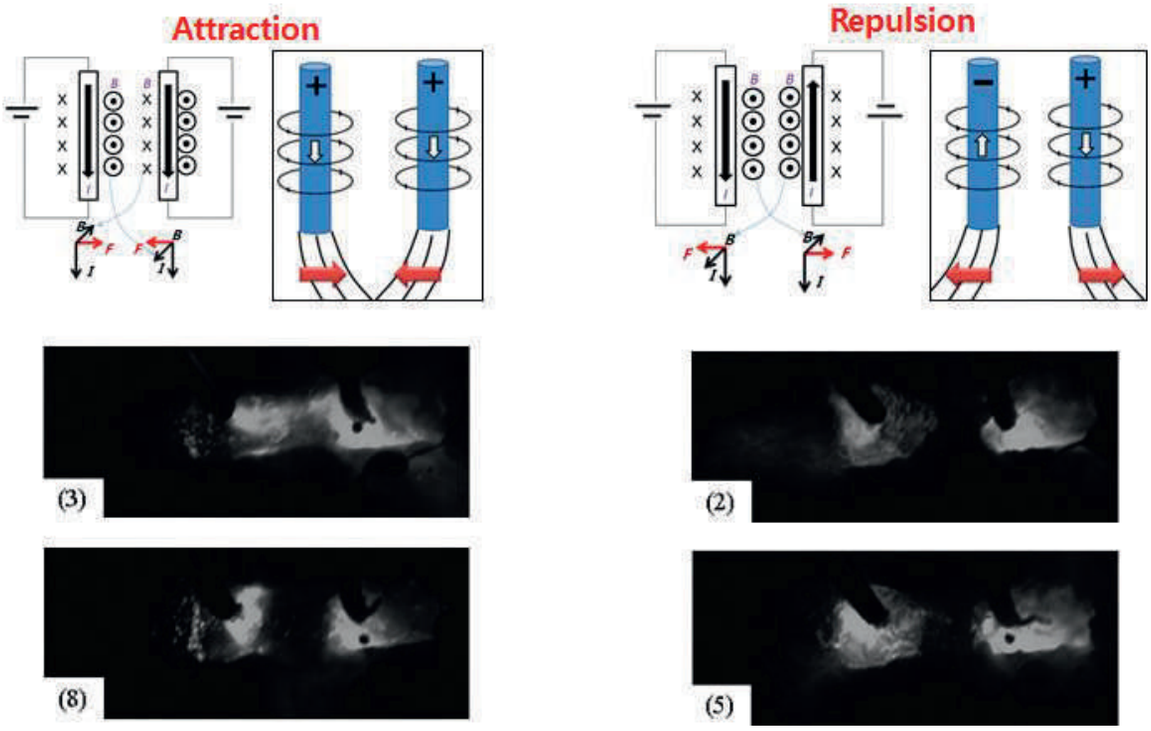

Figure 8. Arc interaction effect of the two wire tandem SAW [17, 28].

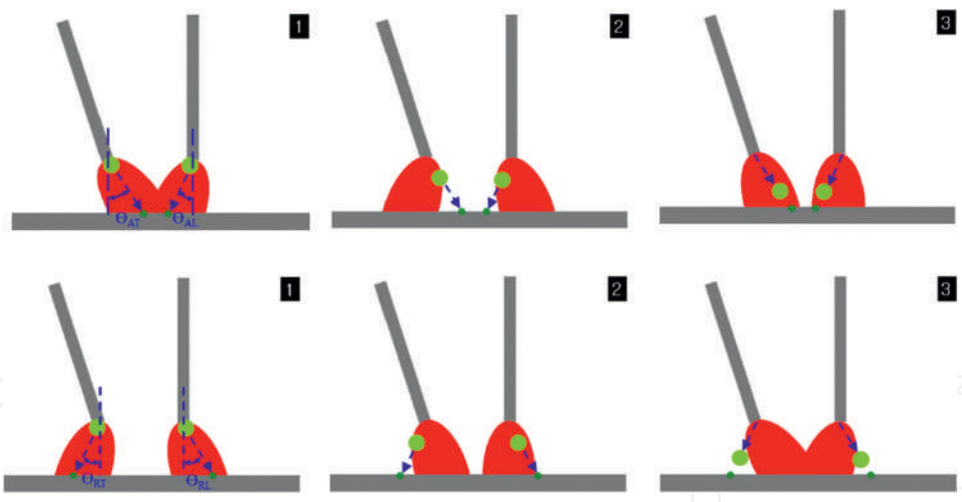

Figure 9. Droplet flights due to the arc interaction effect in two wire SAW process [18].

$$F_{rL} = J_{zL} B_{\theta L} \tag{36}$$

$$F_{zL} = J_{rL} B_{\theta L} \tag{37}$$

$$J_{zT} = \frac{I}{2\pi} \int_0^\infty \lambda J_0(\lambda r_a) \exp\left(-\lambda^2 \sigma_{AT}^2 / 4 d_a\right) \frac{\sinh\left[\lambda(c-z)\right]}{\sinh\left(\lambda c\right)} d\lambda \tag{38}$$

http://dx.doi.org/10.5772/intechopen.76725

$$J_{rT} = \frac{I}{2\pi}\int_0^\infty \lambda J_1(\lambda r_a)\exp\left(-\lambda^2\sigma_{AT}^2/4d_a\right)\frac{\cosh\left[\lambda(c-z)\right]}{\sinh\left(\lambda c\right)}d\lambda \tag{39}$$

$$B_{\theta T} = \frac{\mu_m I_T}{2\pi}\int_0^\infty J_1(\lambda r_a)\exp\left(-\lambda^2\sigma_{AT}^2/4d_a\right)\frac{\sinh\left[\lambda(c-z)\right]}{\sinh\left(\lambda c\right)}d\lambda \tag{40}$$

$$F_{rT} = J_{zT}B_{\theta T} \tag{41}$$

$$F_{zT} = J_{rT}B_{\theta T} \tag{42}$$

2.2.4. Other models

The same surface tension and buoyance force models in equation (24) and (25) are applied.

3. Simulation results for SAW process

3.1. Single wire SAW process

3.1.1. Spray mode of metal transfer

- Single DC

Cho et al. [15] simulated the molten pool behaviors for single DC SAW process which compared the molten pool behaviors for different electrode angles as shown in **Figure 10**. They found that electrode angle plays on important role to form the bead shapes such as penetration and bead width.

When the negative electrode angle is applied, the penetration of weld bead increases deeper because the droplet impingement direction is very similar to the molten poo circulation. Thus the momentum can be transferred sufficiently to the weld pool. Specifically, the molten pool flows downward and backward in the dotted box between droplet generations (**Figure 11(a)** and **(b)**) and then forms a sharp and deep penetration on a transverse cross-section by convection heat transfer as shown in **Figure 12(a)**. However, the positive electrode angle induces

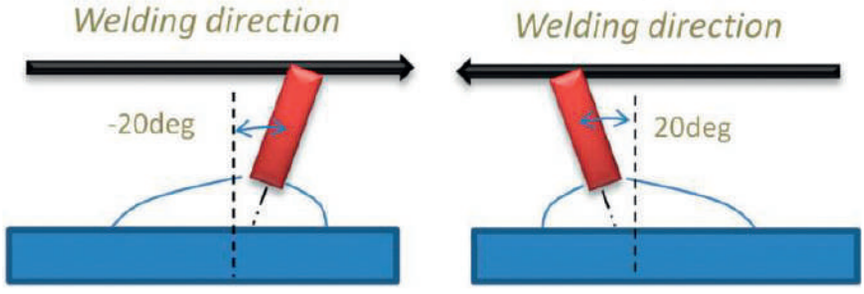

Figure 10. Electrode angle used in the simulation [28].

somewhat different flow patterns because the droplet impingement direction does not match the molten pool direction as shown in **Figure 13(a)** and **(b)**. Therefore, less momentum from the droplet impingement can be transferred in positive electrode angle compared to negative electrode angle.

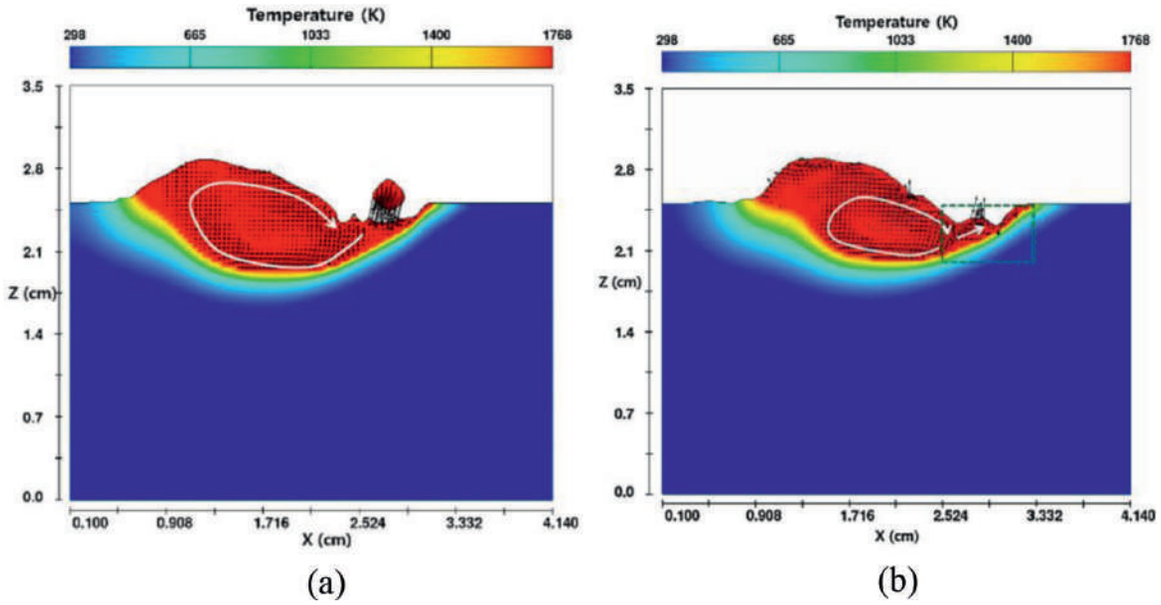

Figure 11. Calculated temperature profiles and flow patterns on a longitudinal cross section for negative electrode angle (−20°C) [15] (a) 0.528 s (b) 0.538 s.

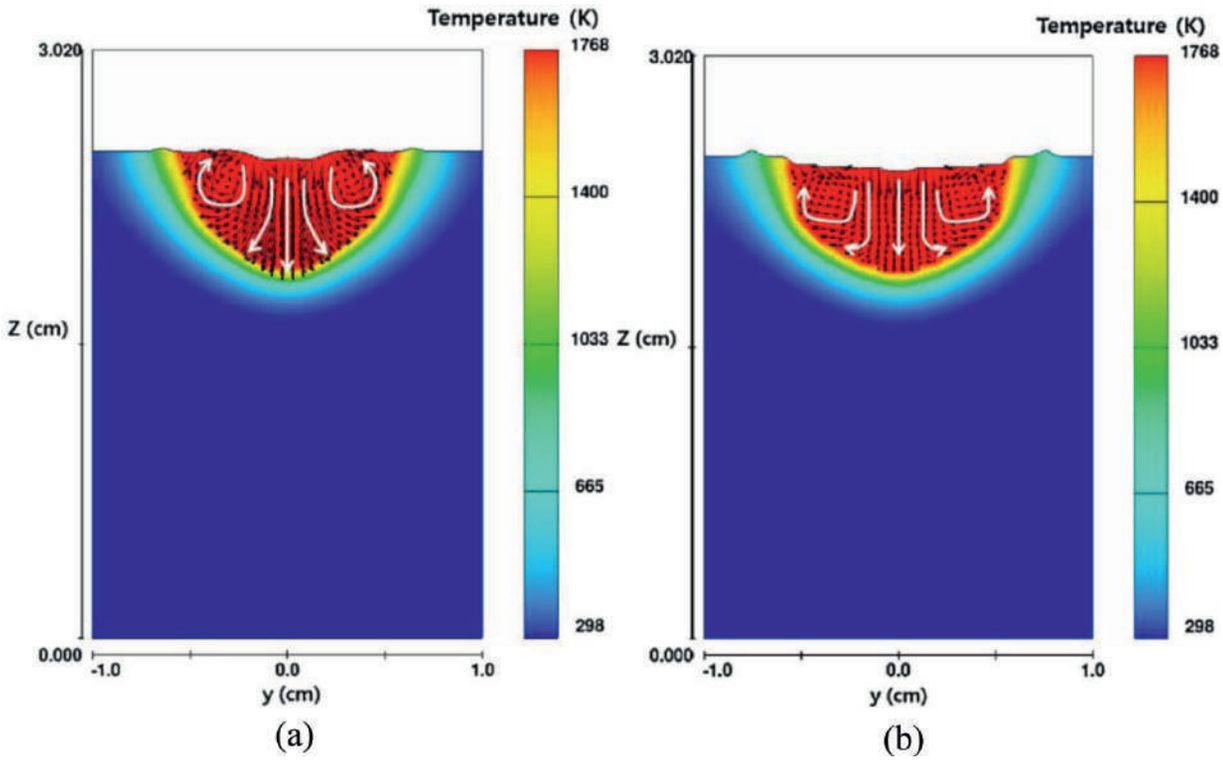

Figure 12. Calculated temperature profiles and flow patterns on a transverse cross section at 0.598 s for negative and positive electrode angle [15] (a) negative angle (−20°) (b) positive angle (+20°).

http://dx.doi.org/10.5772/intechopen.76725

AC welding signals can bring the different simulation results. Cho et al. [15] simulated the molten pool simulation with sinusoidal AC waveform with a negative electrode angle. As the arc shape and signals vary with the welding time, it could induce more dynamic molten pool flows than DC welding. Normally, the frequency of droplet impingement and welding signals cannot be the same so the molten pool under the arc flows forward and backward repeatedly with a welding time as shown in **Figure 14**.

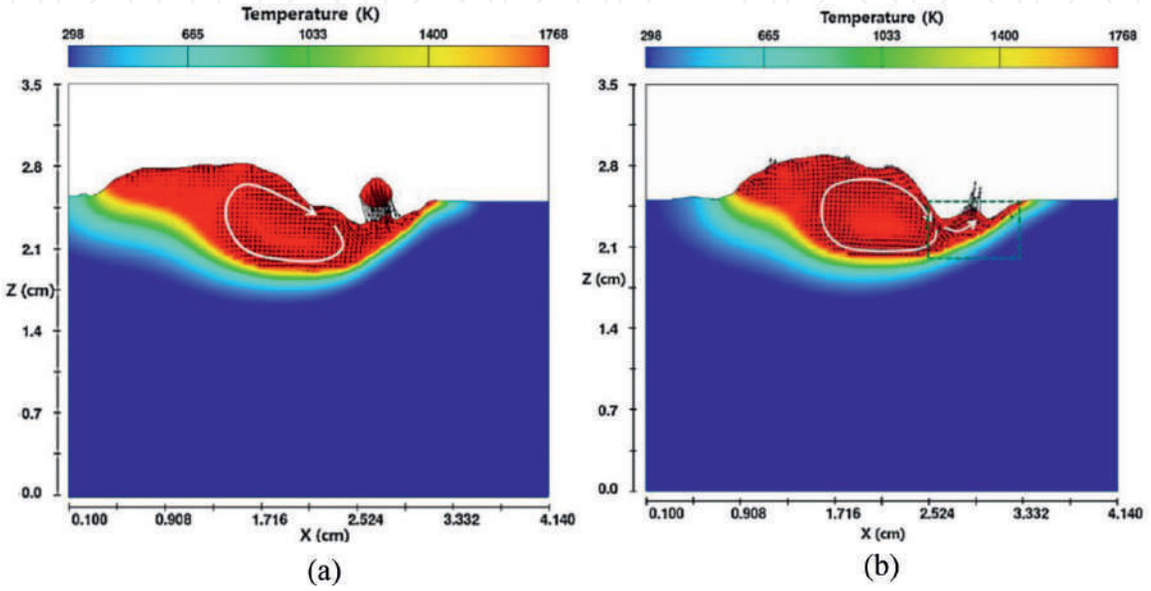

Figure 13. Calculated temperature profiles and flow patterns on a longitudinal cross section for positive electrode angle (+20°C) [15] (a) 0.528 s (b) 0.538 s.

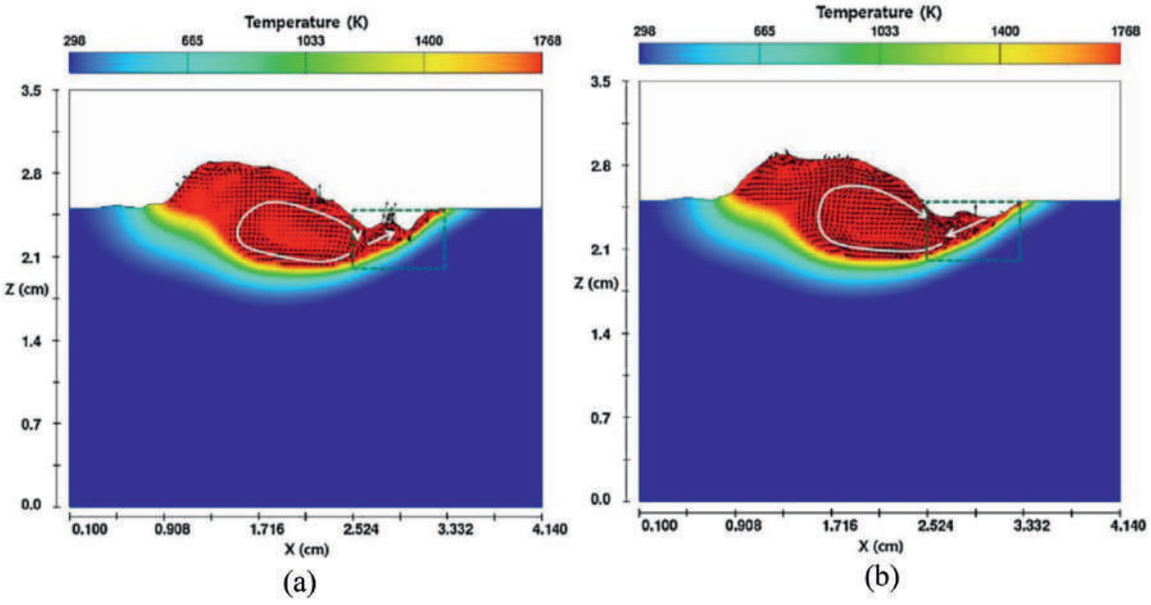

Figure 14. Calculated temperature profiles and flow patterns on a longitudinal cross section for sinusoidal AC waveform (current, voltage) with a negative electrode angle [15] (a) 0.528 s (b) 0.538 s.

When the welding current value is not enough to form the spray metal transfer, it is possible to expect FWG metal transfer mode. Cho et al. [16] simulated the molten pool behavior of FWG metal transfer in V-groove SAW process. The molten droplet impinges to the inner wall boundary and then moves to the V-groove joint sequentially as shown in **Figure 15**. The V-groove joint hardly melts because the arc heat and arc forces (arc pressure & EMF) are not focused on the V-groove joint and. Therefore, it is expected that the inclined side surface melts while the molten pool behavior induces the void in the V-groove joint.

3.2. Multi-wire SAW process

3.2.1. Two wire tandem SAW

Kiran et al. [17] found that when the absolute current value was higher, the arc stiffness increased; thus, the arc tended to be fixed. However, when the absolute current value of the opposite electrode is higher, the arc stiffness decreases, so the arc tends to move backward or forward by the Lorentz force. Finally, the combination of current values from each electrode affects the arc center locations and droplet free flights [18]. For instance, the higher absolute current value can result in an increase in the wire feed rate, which can induce a frequent droplet impingement and a concentration of the arc heat and arc forces.

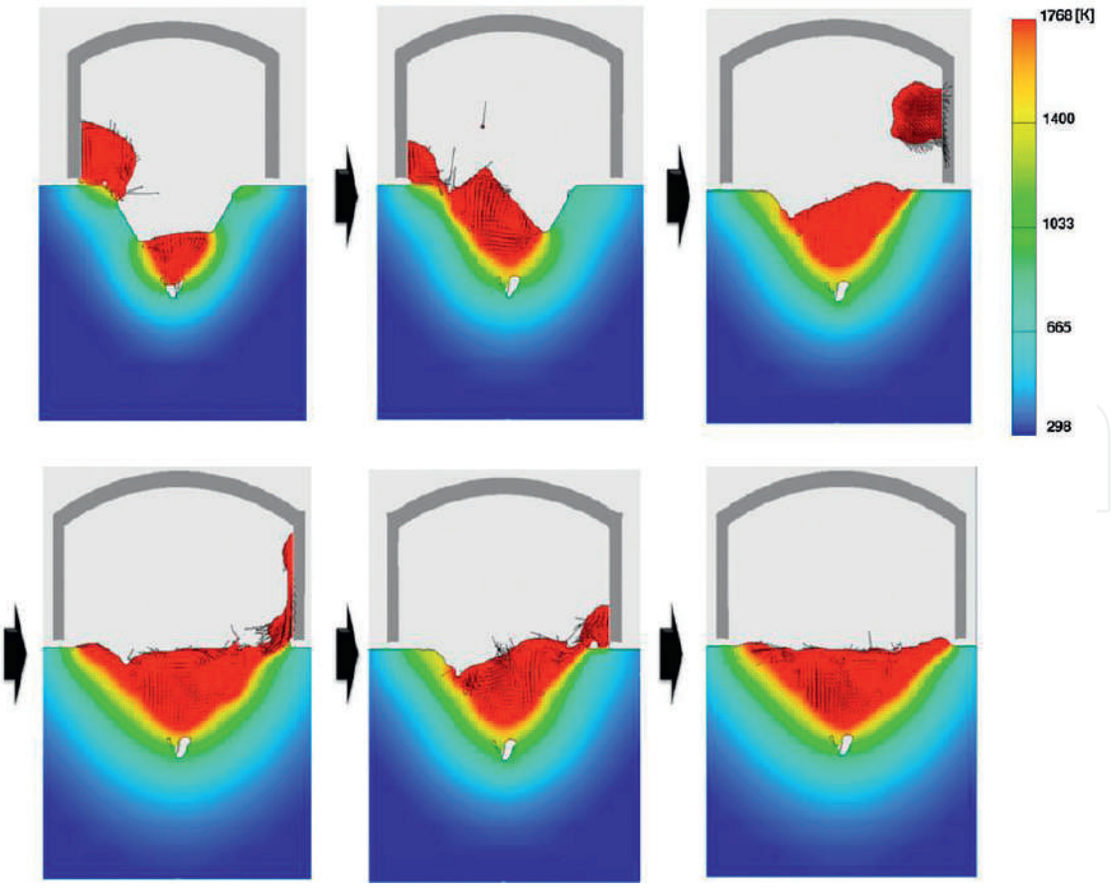

Figure 15. Temperature profiles and flow distributions on the transverse cross section in FWG mode [16].

http://dx.doi.org/10.5772/intechopen.76725

Using this principle, Cho et al. [18] performed CFD simulations and analyzed the results. For higher current in the leading electrode, the arc center displacement of the leading electrode is very small; moreover, the arc heat, arc force and droplet impingement can be focused under the leading electrode. Therefore, the volume of the molten pool ahead of the leading electrode is very small because droplets do not fly ahead of the leading electrode as shown in **Figure 16(a)**.

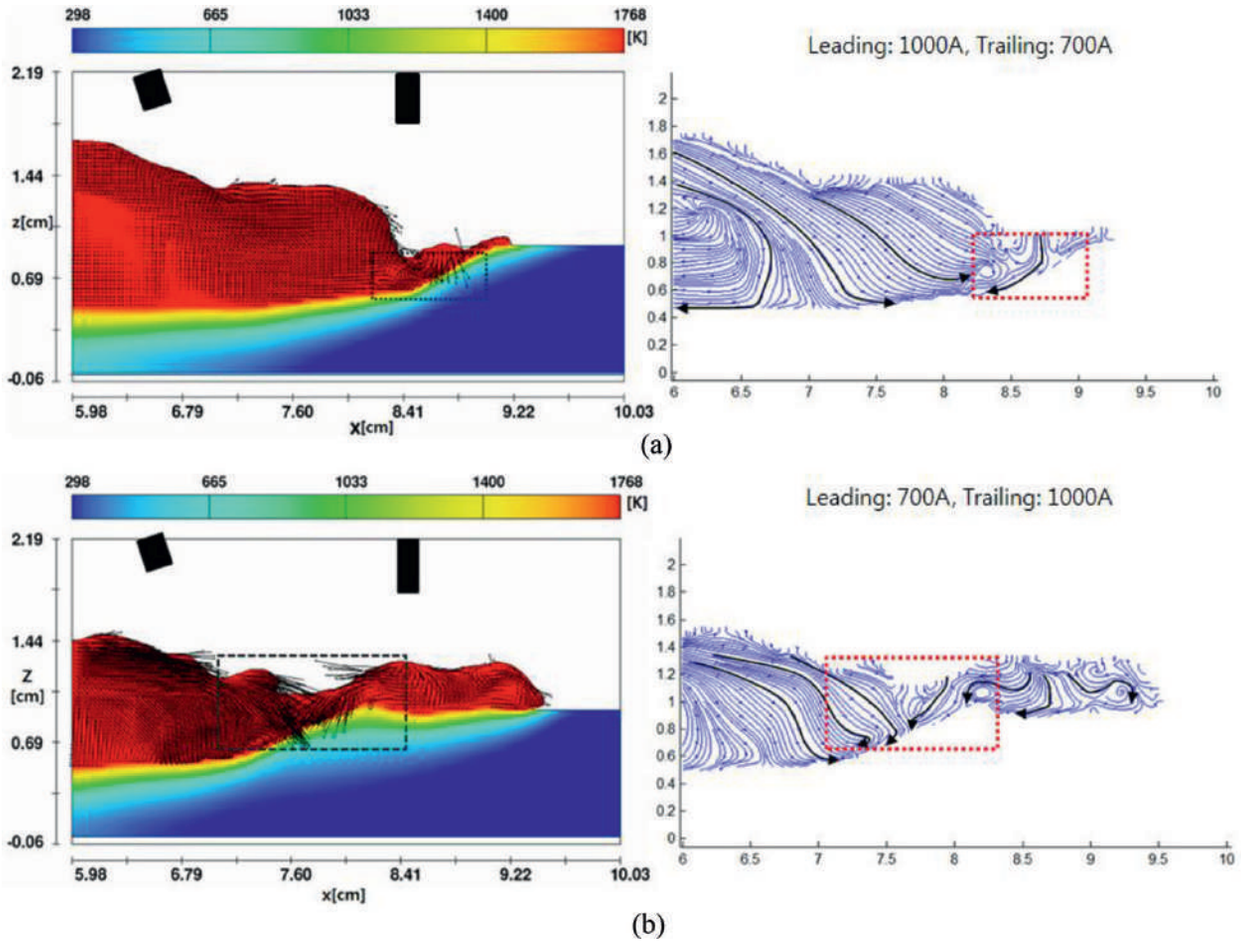

Figure 16. Temperature profiles and streamlines on the longitudinal cross section for two wire tandem SAW process [18] (a) higher current in the leading electrode (b) higher current in the trailing electrode.

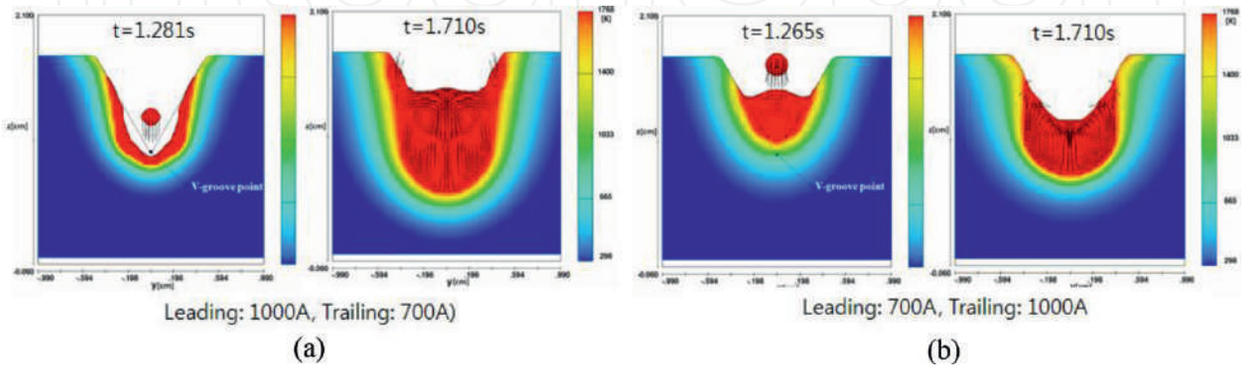

Figure 17. Temperature profiles and streamlines on the transverse cross section for two wire tandem SAW process [18] (a) higher current in the leading electrode (b) higher current in the trailing electrode.

In the transverse section, droplets from the leading electrode impinged on the weld pool whose height is lower than the initial V-grove point; therefore, deep penetration can be from as shown in **Figure 17(a)**. Moreover, the weld pool flows long after droplet impingement in the longitudinal section so this can be another reason to make the deep penetration due to the dynamic convection heat transfer. On the contrary, when the higher current welding signal in the trailing electrode is applied, the arc center displacement of the leading electrode due to the arc

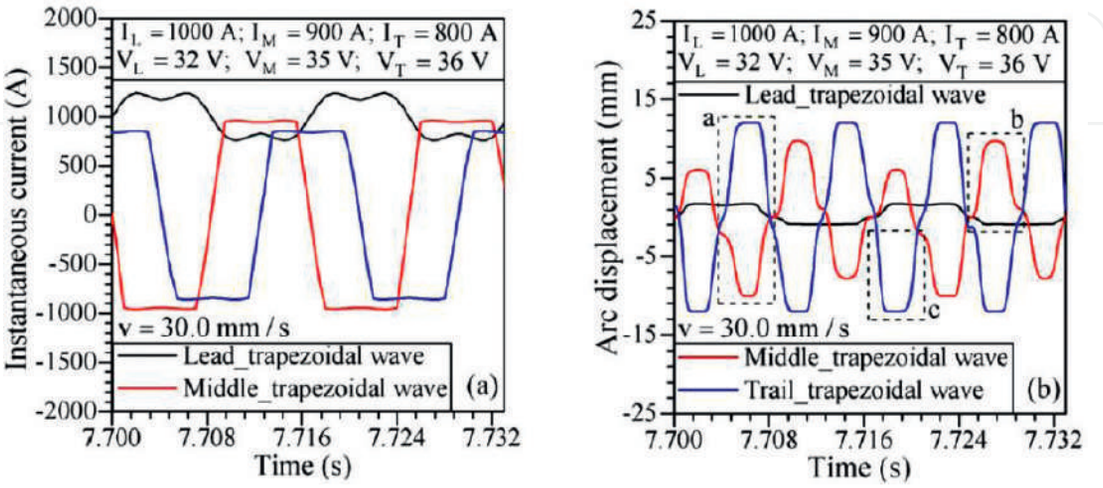

Figure 18. Current waveforms and the corresponding arc center displacement for three wire tandem SAW process [21].

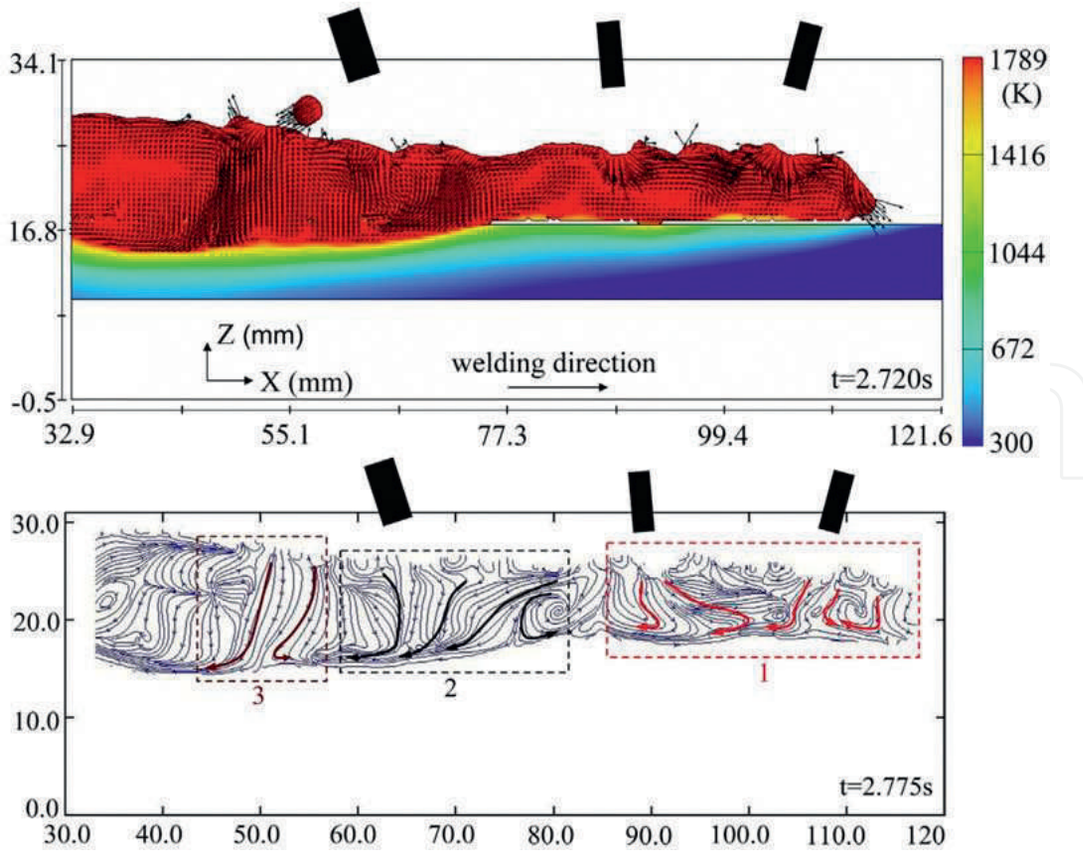

Figure 19. Temperature profiles and streamlines on the longitudinal cross section for three wire tandem SAW process [21].

http://dx.doi.org/10.5772/intechopen.76725

interaction is much bigger than that of the trailing electrode. Therefore, the droplets, arc heat and arc forces from the leading electrode cannot be focused on a similar weld pool spot, but the droplets disperse forward or backward of the welding direction and the form the volume of the molten pool ahead of the leading electrode as shown in **Figure 16(b)**. With these fluid behaviors, the molten pool can fill in the V-groove point; therefore, the molten pool penetrates to a lesser degree than in the higher current in the leading electrode (**Figure 17(b)**).

3.2.2. Three wire tandem SAW

Kiran et al. [21] modeled and simulated the molten pool flow behavior for three wire tandem SAW in V-groove. They firstly measured welding signals and the arc interaction position of three wire SAW process as shown in **Figure 18** and they found that the molten pool behavior from the arc interaction played an important role to increase the penetration of V-groove. It is evident that the middle and trailing arcs are closely concentrated during the attraction (dotted box 'a') compared to that of the same between leading and middle arcs (dotted box 'b'). When the distances of middle and trailing arcs are short (dotted box 'a'), the focused arc heat and arc forces activate the molten pool behavior more dynamic and these increase penetration in the

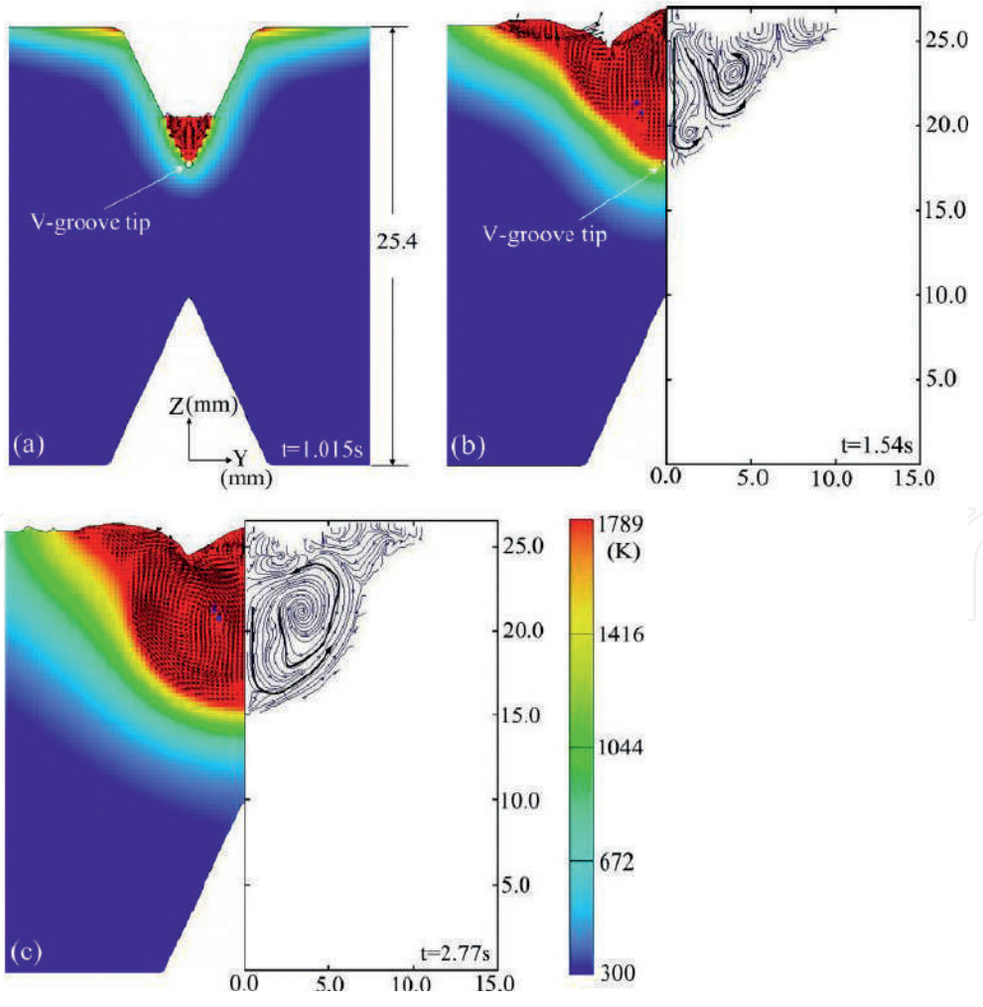

Figure 20. Temperature profiles and streamlines on the transverse cross section for three wire tandem SAW process [21].

longitudinal cross section as shown in **Figure 19**. The molten pool flow patterns in the transverse section are also described in **Figure 20**.

Acknowledgements

The authors gratefully acknowledge the support from Korea Ministry of Trade, Industry and Energy (No.10076430).

Author details

Dae-Won Cho

Address all correspondence to: chodaewon@gmail.com

Busan Machinery Research Center, Korea Institute of Machinery and Materials, Republic of Korea

References

[1] Wen SW, Hilton P, Farrugia DCJ. Finite element modelling of a submerged arc welding process. Journal of Materials Processing Technology. 2001;**119**(1–3):203-209

[2] Sharma A, Chaudhary AK, Arora N, Mishra BK. Estimation of heat source model parameters for twin-wire submerged arc welding. The International Journal of Advanced Manufacturing Technology. 2009;**45**(11–12):1096

[3] Mahapatra MM, Datta GL, Pradhan B, Mandal NR. Three-dimensional finite element analysis to predict the effects of SAW process parameters on temperature distribution and angular distortions in single-pass butt joints with top and bottom reinforcements. International Journal of Pressure Vessels and Piping. 2006;**83**(10):721-729

[4] Kiran DV, Basu B, Shah AK, Mishra S, De A. Three-dimensional heat transfer analysis of two wire tandem submerged arc welding. ISIJ International. 2011;**51**(5):793-798

[5] Kim JW, Na SJ. A study on the three-dimensional analysis of heat and fluid flow in gas metal arc welding using boundary-fitted coordinates. Journal of Engineering for industry. 1994;**116**(1):78-85

[6] Kim CH, Zhang W, DebRoy T. Modeling of temperature field and solidified surface profile during gas–metal arc fillet welding. Journal of Applied Physics. 2003;**94**(4):2667-2679

[7] Kim WH, Fan HG, Na SJ. Effect of various driving forces on heat and mass transfer in arc welding. Numerical Heat Transfer, Part A Applications. 1997;**32**(6):633-652

[8] Cho DW, Na SJ, Cho MH, Lee JS. Simulations of weld pool dynamics in V-groove GTA and GMA welding. Welding in the World. 2013;**57**(2):223-233

[9] Cho DW, Na SJ, Cho MH, Lee JS. A study on V-groove GMAW for various welding positions. Journal of Materials Processing Technology. 2013;**213**(9):1640-1652

[10] Cho DW, Lee SH, Na SJ. Characterization of welding arc and weld pool formation in vacuum gas hollow tungsten arc welding. Journal of Materials Processing Technology. 2013;**213**(2):143-152

[11] Cho JH, Na SJ. Implementation of real-time multiple reflection and Fresnel absorption of laser beam in keyhole. Journal of Physics D: Applied Physics. 2006;**39**(24):5372

[12] Cho JH, Na SJ. Three-dimensional analysis of molten pool in GMA-laser hybrid welding. Welding Journal. 2009;**88**(2):35-43

[13] Han SW, Cho WI, Na SJ, Kim CH. Influence of driving forces on weld pool dynamics in GTA and laser welding. Welding in the World. 2013;**57**(2):257-264

[14] Cho WI, Na SJ, Cho MH, Lee JS. Numerical study of alloying element distribution in CO2 laser–GMA hybrid welding. Computational Materials Science. 2010;**49**(4):792-800

[15] Cho DW, Song WH, Cho MH, Na SJ. Analysis of submerged arc welding process by three-dimensional computational fluid dynamics simulations. Journal of Materials Processing Technology. 2013;**213**(12):2278-2291

[16] Cho DW, Kiran DV, Na SJ. Analysis of molten pool behavior by flux-wall guided metal transfer in low-current submerged arc welding process. International Journal of Heat and Mass Transfer. 2017;**110**:104-112

[17] Kiran DV, Cho DW, Song WH, Na SJ. Arc behavior in two wire tandem submerged arc welding. Journal of Materials Processing Technology. 2014;**214**(8):1546-1556

[18] Cho DW, Kiran DV, Song WH, Na SJ. Molten pool behavior in the tandem submerged arc welding process. Journal of Materials Processing Technology. 2014;**214**(11):2233-2247

[19] Kiran DV, Cho DW, Lee HK, Kang CY, Na SJ. A study on the quality of two-wire tandem submerged arc welds under iso-heat input conditions. The International Journal of Advanced Manufacturing Technology. 2015;**78**(1–4):53-62

[20] Cho DW, Kiran DV, Na SJ. Analysis of the flux consumption and metal transfer for tandem submerged arc welding process under iso-heat input condition. Welding Journal. 2015;**94**: 396-401

[21] Kiran DV, Cho DW, Song WH, Na SJ. Arc interaction and molten pool behavior in the three wire submerged arc welding process. International Journal of Heat and Mass Transfer. 2015;**87**:327-340

[22] Franz U. Vorgange in der Kaverne beim UP-Schweissen Teil I. Schweiss Tech. 1965;**15**:145-150

[23] Van Adrichem JT. Metal transfer in submerged arc welding. International Institute of Welding Document. 1966:212-278

[24] Chandel RS. The effect of process variables on the flux consumption in submerged arc welding. Material and Manufacturing Process. 1998;**13**(2):181-188

[25] Renwick BG, Patchett BM. Operating characteristics of the submerged arc process. Welding Journal. 1976;**55**(3):69

[26] Kou S, Sun DK. Fluid flow and weld penetration in stationary arc welds. Metallurgical Transactions A. 1985;**16**(1):203-213

[27] Sahoo P, DebRoy T, McNallan MJ. Surface tension of binary metal—Surface active solute systems under conditions relevant to welding metallurgy. Metallurgical Transactions B. 1988;**19**(3):483-491

[28] Cho DW. A Study on Molten Pool Flow Behavior in Pipe Seam Welding and Girth Welding Processes by Computational Fluid Dynamics. Kaist Ph. D [Thesis] 2014

IntechOpen

We are IntechOpen, the world's leading publisher of Open Access books
Built by scientists, for scientists

6,300
Open access books available

171,000
International authors and editors

190M
Downloads

Our authors are among the

154
Countries delivered to

TOP 1%
most cited scientists

12.2%
Contributors from top 500 universities

CLARIVATE ANALYTICS
BOOK CITATION INDEX
INDEXED

WEB OF SCIENCE™

Selection of our books indexed in the Book Citation Index in Web of Science™ Core Collection (BKCI)

Interested in publishing with us?
Contact book.department@intechopen.com

Numbers displayed above are based on latest data collected.
For more information visit www.intechopen.com

Chapter 2

Direct Numerical Simulation of Hydrate Dissociation in Homogeneous Porous Media by Applying CFD Method: One Example of CO_2 Hydrate

Wu-Yang Sean

Additional information is available at the end of the chapter

http://dx.doi.org/10.5772/intechopen.74874

Abstract

Computational fluid method (CFD) is popular in either large-scale or meso-scale simulations. One example is to establish a new pore-scale (m~μm) model of laboratory-scale sediment samples for estimating the dissociation rate of synthesized CO_2 hydrate (CO_2H) reported by Jeong. It is assumed that CO_2H formed homogeneously in spherical pellets. In the bulk flow, concentration and temperature of liquid CO_2 in water flow was analyzed by CFD method under high-pressure state. Finite volume method (FVM) were applied in a face-centered packing in unstructured mesh. At the surface of hydrate, a dissociation model has been employed. Surface mass and heat transfer between hydrate and water are both visualized. The initial temperature 253.15K of CO_2H pellets dissociated due to ambient warm water flow of 276.15 and 282.15K and fugacity variation, ex. 2.01 and 1.23 MPa. Three tentative cases with porosity 74, 66, and 49% are individually simulated in this study. In the calculation, periodic conditions are imposed at each surface of packing. Numerical results of this work show good agreement with Nihous' model. Kinetic modeling by using 3D unstructured mesh and CFD scheme seems a simple tool, and could be easily extended to determine complex phenomena coupled with momentum, mass and heat transfer in the sediment samples.

Keywords: heat and mass transfer, finite volume method (FVM), computational fluid dynamics (CFD), pore-scale flow

1. Introduction

Computational fluid method (CFD) is popular in either large-scale or meso-scale simulations. One example is to establish a new pore-scale (m~μm) model of laboratory-scale sediment

IntechOpen

© 2018 The Author(s). Licensee IntechOpen. This chapter is distributed under the terms of the Creative Commons Attribution License (http://creativecommons.org/licenses/by/3.0), which permits unrestricted use, distribution, and reproduction in any medium, provided the original work is properly cited. CC BY

samples for estimating the dissociation rate of synthesized CO_2 hydrate (CO_2H) reported by [1]. To decrease the CO_2 concentration in the air, carbon dioxide capture and storage (CCS) is regarded to be an effective way. One concept of CCS is to store CO_2 in gas hydrate in sub-seabed geological formation, as was illustrated by [6]. Besides, many studies about the formation and dissociation of CO_2 hydrate (CO_2H) while stored in the deep ocean or geologic sediment have been introduced. In particular, flow and transport in sediment is multidisciplinary science including the recovery of oil, groundwater hydrology and CO_2 sequestration. It reported the measurements of the dissociation rate of well-characterized, laboratory-synthesized carbon dioxide hydrates in an open-ocean seafloor [5]. The pore effect in the phase equilibrium mainly due to the water activity change was discussed in [7]. The reactive transport at the pore-scale to estimate realistic reaction rates in natural sediments was discussed in [3]. This result can be used to inform continuum scale models and analyze the processes that lead to rate discrepancies in field applications. Pore-scale model is applied to examine engineered fluids [4]. Unstructured mesh is well suited to pore-scale modeling because of adaptive sizing of target unit with high mesh resolution and the ability to handle complicated geometries [17, 18]. Particularly, it can easily be coupled with computational fluid dynamics (CFD) methods, such as finite volume method (FVM) or finite element method (FEM). Unstructured tetrahedral mesh used to define the pore structure is discussed in [19]. Another case includes a numerical simulation of laminar flow based on FVM with unstructured meshes was used to solve the incompressible, steady Navier-Stokes equations through a cluster of metal idealized pores by [20].

The objective of this work is to develop a new pore-scale model for estimating the dissociation rate of CO_2H in homogeneous porous media. To cooperate with molecular simulation and field-scale simulators, we aim at establishing pore-scale modeling to analyze the simultaneous kinetic process of CO_2H dissociation due to non-equilibrium states. Major assumptions in this study are listed as below:

1. Only dissociation occurred at the surface, no any formation occurred immediately with dissociation.
2. CO_2 dissociated at the surface is assumed to be dissolved into liquid water totally without considering the gas nucleated.
3. The surface structure does not collapse with the dissociation of CO_2H at the surface of pellets.
4. Homogeneous face-centered packing of multi-CO_2H pellets.
5. Single phase flow coupled with mass, heat, and momentum transfers.

2. Dissociation modeling at the surface

In this study, the dissociation flux (F_1) is assumed to be proportional to the driving force, the free energy difference ($\Delta\mu$) introduced by [6], presented as

$$F_1 = k_{\mathrm{bl}} \mathrm{RT} \ln\left(\frac{C_{Hsol}}{C_I}\right) \tag{1}$$

http://dx.doi.org/10.5772/intechopen.74874

where k_{bl} is the rate constant $\left[\text{mol}^2\ \text{J}^{-1}\ \text{s}^{-1}\text{m}^{-2}\right]$ of dissociation. According to [21], k_{bl} is listed as below:

$$k_{bl} = \exp\left(-\frac{11,729}{T} + 26.398\right) \tag{2}$$

where C_{Hsol} is the mole fraction of CO_2 in the aqueous solution at equilibrium state with hydrate, and C_I means surface concentration in the ambient aqueous solution at the surface of the hydrate C_I.

3. Basic transport equations

Flow in the porous media around CO_2H is governed by the continuity and the Navier-Stoke's equations. The advection-diffusion equations of non-conservative type for mass concentration C and temperature T are also considered.

$$\nabla \cdot \mathbf{u} = 0 \tag{3}$$

$$\frac{\partial \mathbf{u}}{\partial t} + \nabla \cdot (\mathbf{uu}) = -\nabla P + \frac{1}{\text{Re}} \nabla \cdot \left[\nabla \mathbf{u} + (\nabla \mathbf{u})^T\right] + \frac{\rho_w}{\text{Fn}^2} g \tag{4}$$

No.	Function	Definition
1	$D = 7.4 \times 10^{-12} \frac{(\varphi M_B)^{1/2} T}{\eta_L V_A^{0.6}}$	D: diffusion coefficient of CO_2 in water φ(=2.6): association parameter for the solvent water $M_B\left(= 18\ \text{gmol}^{-1}\right)$: molecular weight of water $V_A\left(= 3.4 \times 10^{-5}\ \text{m}^3\text{mol}^{-1}\right)$: molar volume of CO_2 η_L[mPa·s]: viscosity of water
2	$\nu_L = \left(8.8286 \times 10^{-10}\right)T^2 - \left(5.3886 \times 10^{-7}\right)T + 8.314 \times 10^{-5}$	$\nu_L\left[\text{ms}^{-2}\right]$: kinematic viscosity
3	$\lambda_L = 487.85\ln(T) - 2173.8$	$\lambda_L\left[\text{WKm}^{-1}\right]$: heat conductivity of water
4	$\alpha_L = \frac{\lambda_L}{\rho_W C_p}$	$\alpha_L\left[\text{ms}^{-2}\right]$: the thermal diffusivity of aqueous phase $\rho_W\left(= 997.1 \frac{\text{kg}}{\text{m}^3}\right)$: density of water $C_p\left(= 4,180 \frac{\text{J}}{\text{kg}} \cdot \text{K}\right)$: isobaric specific heat, quoted from "Chemical Engineering Handbook", Japan (1985)
5	$P_{eq} = \exp\left(\alpha + \frac{\beta}{T}\right) \times 10^3$	α=44.580 and β = − 10246.28
6	$C_{Hsol} = a \cdot \exp\left(b \cdot P \times 10^{-6} + 1.321 \times 10^{-4} T - 2.292 \times 10^{-2}\right) \cdot 1.8 \times 10^{-5}$	$C_{Hsol}\left[\text{mole} \cdot \text{m}^{-3}\right]$: solubility of hydrate (275.15 K < T < 281.15 K) $a = 0.0016(T - 273.15)^{0.9211}$ $b = -0.0199\log(T - 273.15) + 0.0942$ by Aya et al. [10], Yang et al. [11], and Servio and Englezos [12]

Table 1. Parameters used in this study.

$$\frac{\partial C}{\partial t} + \mathbf{u} \cdot \nabla C = \frac{1}{\mathrm{ReSc}} \nabla^2 C \tag{5}$$

$$\frac{\partial T}{\partial t} + \mathbf{u} \cdot \nabla T = \frac{1}{\mathrm{RePr}} \nabla^2 T \tag{6}$$

where the viscosity, diffusivity, and thermal conductivity of pure water are included in dimensionless parameters such as the Reynolds number, the Schmit number, and the Prandtl number, which are interpolated as functions of temperature and are updated at every computational time step as summarized in **Table 1**. U and d (=0.001 m) are the velocity of inflow and diameter of hydrate pellet.

4. Mass transfer

To rewrite Eq. (1), the flux at the surface of the hydrate can be discretized as

$$k_{bl} RT \ln\left(\frac{C_{Hsol}}{C_I}\right) = D\nabla C = D\frac{C_I - C'}{h_I} \tag{7}$$

where C_I is the varying surface concentration calculated locally at each surface cell, C' is the centroid concentration, and h_I is the thickness of centroid surface cell, as shown in **Figure 1**.

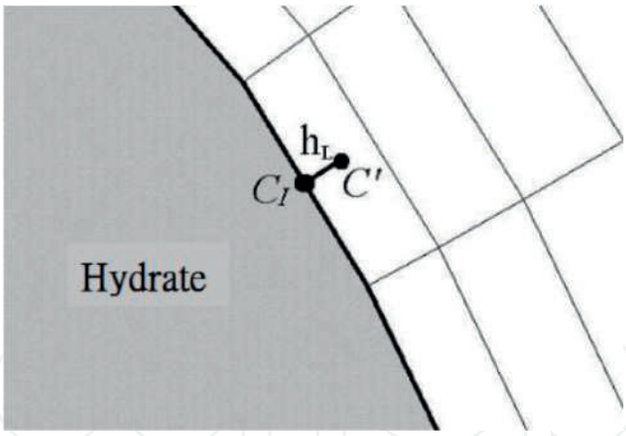

Figure 1. Schematic image of discretized surface concentration.

5. Heat transfer

The equation of energy balance at the surface of CO_2H is given by

$$\dot{Q}_H + \lambda_H \nabla T_H = \lambda_L \nabla T_L \tag{8}$$

http://dx.doi.org/10.5772/intechopen.74874

where $\dot{Q}_H$ (= $H_L F_1$, where H_L is the latent heat of hydrate dissociation) is the dissociation heat transferred to the CO_2H, λ_H is the thermal conductivity of hydrate. Dissociation heat per mole of hydrate, H_L, is interpolated from [2] as

$$H_L = 207,917 - 530.97 \times T_I \tag{9}$$

where T_I is the surface temperature. Then, we have

$$T_I = \frac{\lambda_L h_H T_L + \lambda_H h_L T_H - 207,917 \cdot F_{cal} h_L h_H}{\lambda_L h_H + \lambda_H h_L - 530.97 \cdot F_{cal} h_L h_H} \tag{10}$$

where T_L and T_H are the temperatures defined at the centroids cell in the aqueous phase and solid hydrate, respectively; h_L and h_H are half widths of centroid in the aqueous phase and solid hydrate, respectively. Besides, the temperature in the pellet is calculated by using the heat conductivity equation.

$$\frac{\partial T}{\partial t} = \alpha_H \frac{\partial^2 T}{\partial x^2} \tag{11}$$

where $\alpha_H = \frac{\lambda_H}{\rho_H C_p'}$ is the thermal diffusivity of CO_2H. These relative properties of CO_2H are quoted from [9], the thermal diffusivity of aqueous phase (α_H) of $1.38 \times 10^{-7} ms^{-2}$, the heat capacity of hydrate (C_p') of $2080.0\ JK^{-1}kg^{-1}$, and the thermal conductivity (λ_H) of $0.324\ WK^{-1}m^{-1}$. The density of CO_2H (ρ_H) is given as $1116.8\ kgm^{-3}$.

6. Computational conditions

Two types of cells, tetrahedrons and triangular prisms, are applied in the present unstructured grid system, as introduced in **Figure 2**. In detailed, the surface of hydrate uses prism. Both the flow field and inside the pellet are tetrahedral meshes. Upward is the inflow where initially the uniform velocity profile is adopted. Prism mesh and no-slip condition are imposed at the surface of the pellet. To analyze more detailed mass and heat transfer simulatneously, one cell-layer of the prisms that attached to the CO_2H surface is divided into at least five very thin layers as referred in [8] for high Prandtl or Schmidt number. The basic parameters of computation are denoted in **Table 1**. The initial values of dimensionless parameters are listed in **Table 2** at the temperatures from 276.15 to 283.15 K. Reynolds number, Schmidt number, and Prandtl number function of the temperature or pressure are listed in **Table 2**. The minimum grid size of this computational model is listed in **Table 3**. Lm, Lc, and LT are the applied mesh thicknesses. δm, δc, and δT are the thickness of momentum, concentration, and thermal boundary layers, respectively. The relationship between δm, δc, and δT quoted from the theory of flat plate boundary layer is listed below:

$$\delta_m = \frac{5.48}{\sqrt{\mathrm{Re}}}\frac{d}{2} \tag{12}$$

$$\delta_c = \frac{\delta_m}{1.026 \cdot Sc^{1/3}} \tag{13}$$

$$\delta_T = \frac{\delta_c}{\mathrm{Pr}^{1/3}} \tag{14}$$

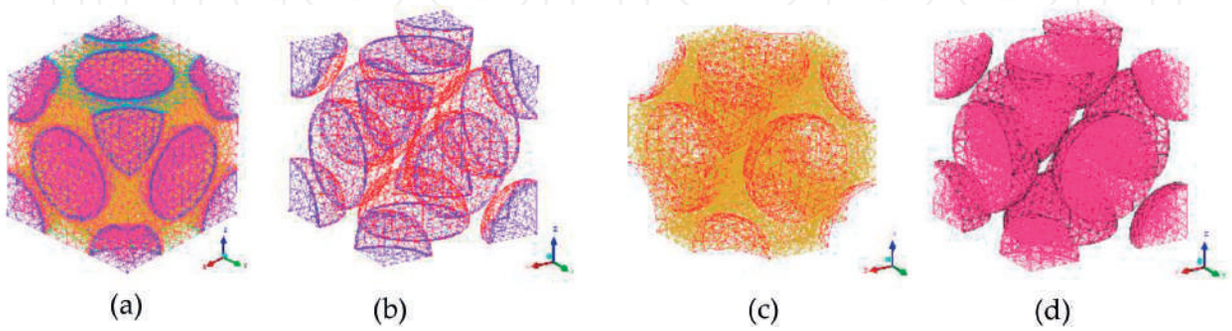

Figure 2. Description of mesh in unstructured grid system of 67,104 cells. (a) Overview, (b) surface of CO_2H, (c) water, and (d) pellets of CO_2H.

Case	Reynold number	Prandtl number	Froude number	Schmidt number	Porous ratio	Temperature of water (K)	Fugacity of equilibrium (MPa)	Fugacity (MPa)
1	50	10	0.023	755	74%	282.15	3.89	3
2		12		880		276.15	1.77	1
3		10		755	66%	282.15	3.89	3
4		12		880		276.15	1.77	1
5		10		755	49%	282.15	3.89	3
6		12		880		276.15	1.77	1
7	100	10	0.046	755		282.15	3.89	3
8	135		0.062					

Table 2. Calculation conditions of this work.

Cell number (porosity)	Sc*	δ_m*	$\delta_{c\&T}$*	L_m	VTL number	$L_{c\&T}$
53,440 (49%)	755	2.358E-04	2.252E-05	1.0E-05	5	2.0E-06
67,104 (66%)	755	2.345E-03	2.252E-04	6.0E-05	5	1.2E-05
77,432 (74%)	755	2.594E-03	2.276E-04	6.0E-05	5	1.2E-05

*Values are quoted from "Chemical Engineering Handbook", Japan (1985)

Table 3. The thicknesses of boundary layers, δ_m and $\delta_{c\&T}$, and grid sizes, L_m and $L_{c\&T}$ (unit: meter).

http://dx.doi.org/10.5772/intechopen.74874

To follow [22] of Eq. (14), the boundary layer's thickness for temperature, δ_T is assumed as the same size as that for mass concentration, δ_c. For the initial temperature of the CO_2H pellet, T_{ini} is assumed as a constant value of 253.15 K.

7. Verification

The in-house code originally developed by [7] has been applied to determine the intrinsic dissociation rate of methane hydrate. The numerical results verified by experimental results are successfully used in calculating one pellet of hydrate in a slow flow rate of high pressure without considering the collapse of hydrate and the nucleation of bubbles referring to [6, 20] as well.

8. Results of case study

In this study, cases with porosity of 74, 66, and 49 are individually discretized as face-centered unstructured packing of hydrate in sediment. CO_2H pellets with initial temperature of 253.15 K dissociate due to the variation of driving force, ex. 0.89 and 0.77 MPa, under thermal stimulation of ambient warm water, ex. 282.15 and 276.15 K. Comparative small driving forces selected here is due to the assumption of no surface's collapse. Computational conditions are listed in **Table 2**. Result of flux at the surface is the converge value as shown in **Figure 3**. In **Figure 4(a)–(c)** at time 0.16(s) show velocity vector of case 1 in three specific sections. In **Figure 5**, the distributions of concentration at 0.16 s are presented. Slight CO_2 discharges at the surface. Relative temperature distributions are indicated in **Figure 6**. As time increases, the dissociation heat of CO_2 hydrate results in water temperature drop significantly as shown in

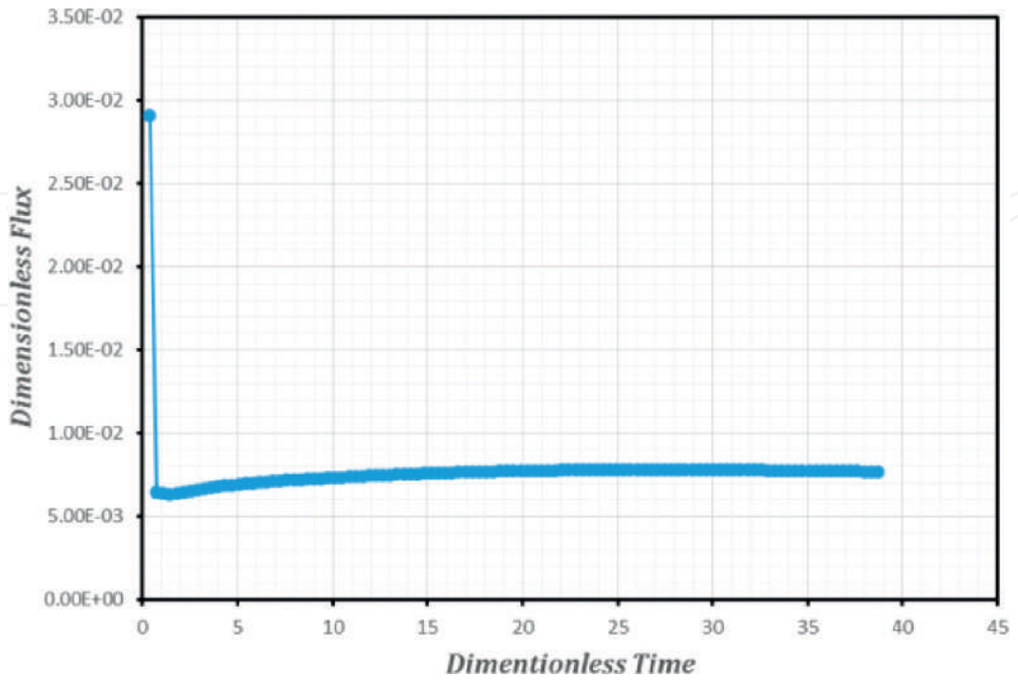

Figure 3. Converge value of case 1.

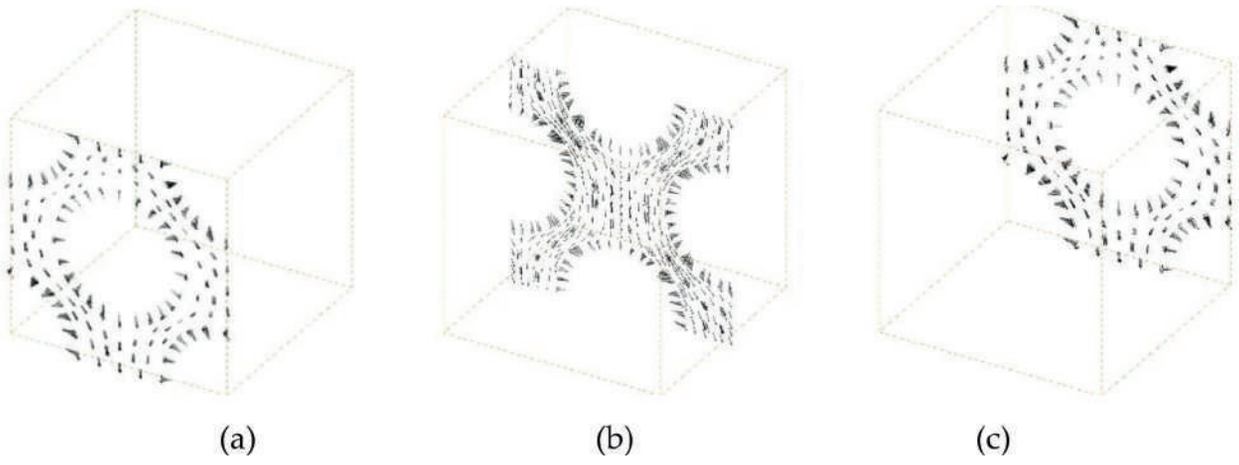

Figure 4. Velocity vector in the vicinity of pellets (case 1: T = 282.15 K, T_{ini} = 253.15 K, Re = 50, Sc = 755, Pr = 10, VTL = 5, and time = 0.16 s). (a) Front section, (b) Center section and (c) Back section.

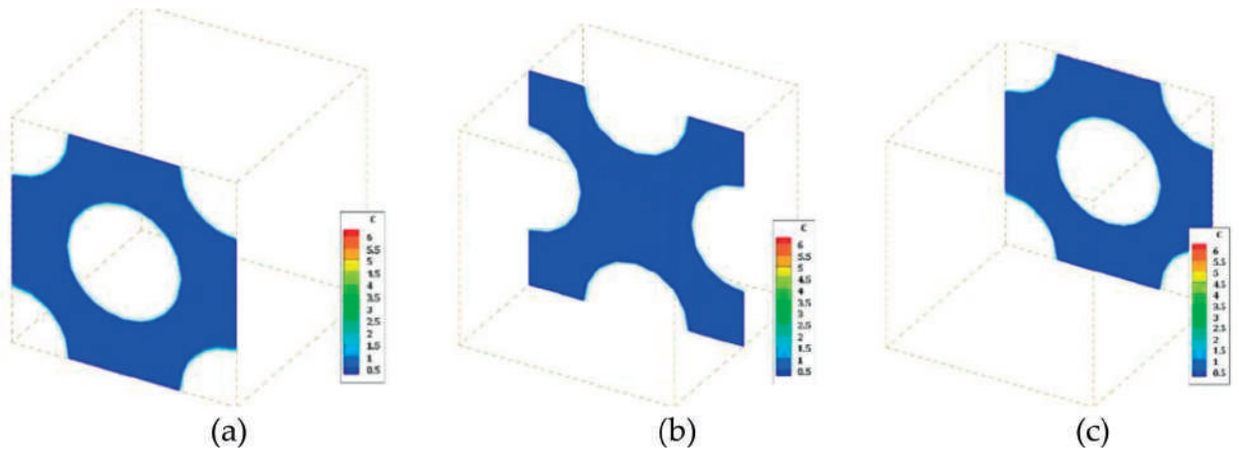

Figure 5. Concentration profile in three specific sections of cubic unit (case 1: time = 0.16 s, unit: mole/m^2 s). (a) Front section, (b) Center section and (c) Back section.

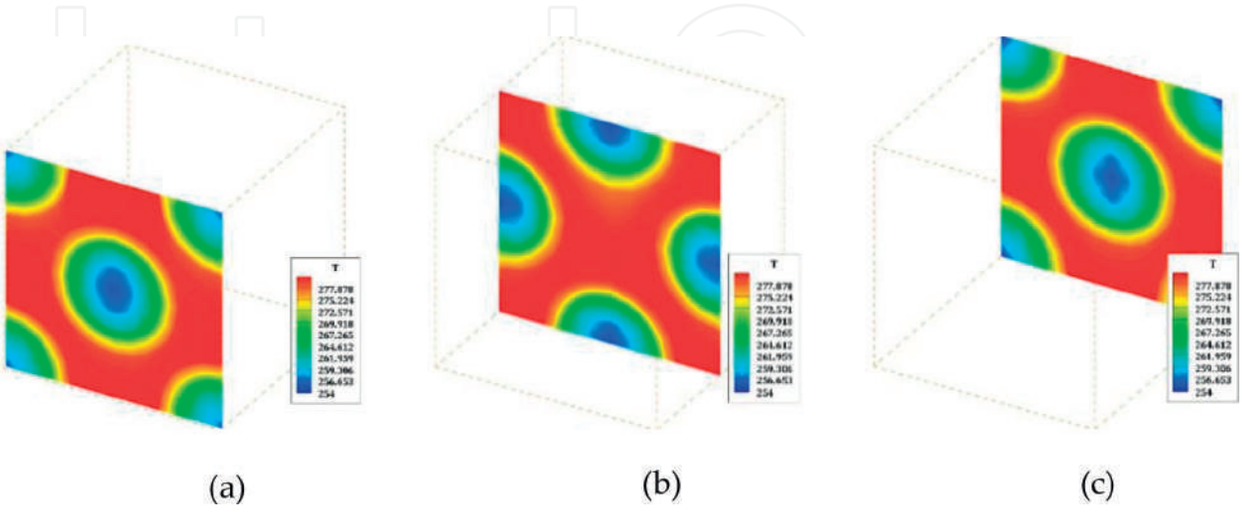

Figure 6. Temperature profile in three specific sections of cubic unit (case 1, time = 0.16 s, unit: K). (a) Front section, (b) Center section and (c) Back section.

http://dx.doi.org/10.5772/intechopen.74874

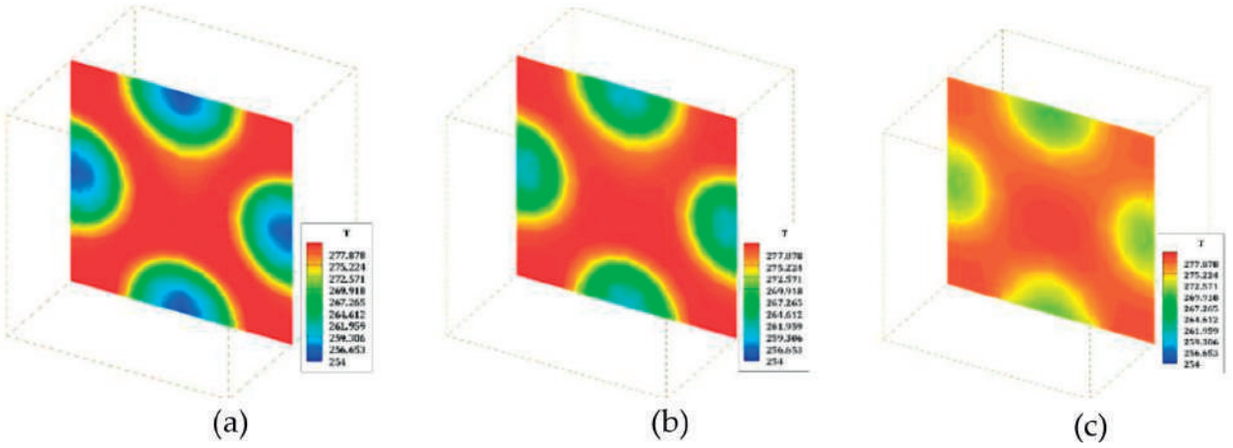

Figure 7. Temperature versus time in center section of cubic unit (case 1, time = 0.16 s, 0.27 s, and 0.54 s, unit: K). (a) Front section, (b) Center section and (c) Back section.

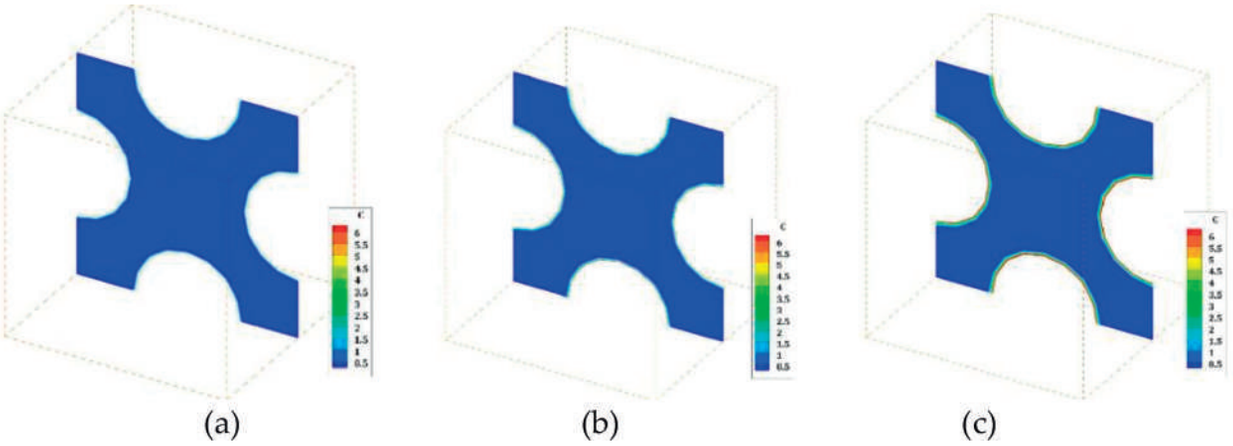

Figure 8. Concentration versus time in center section of cubic unit (case 1, time = 0.16 s, 0.27 s, and 0.54 s, unit: mole/m^2 s). (a) Front section, (b) Center section and (c) Back section.

Figure 7(a)–(c). Relative concentration distribution in center section is shown in **Figure 8**. The heat of water conducts to the solid-side pellet rapidly in few seconds, and slow mass transfer at the surface dominates the dissociation rate rather than fast heat transfer at the surface.

9. Discussion

To follow the modeling illustrated in [14]:

$$F_3 = k_D\left(f_{eq} - f_g\right) = k_{D0}\exp\left(-\frac{\Delta E}{RT}\right)\left(f_{eq} - f_g\right) \tag{15}$$

where $k_{D0}\left[\text{mol Pa}^{-1}\text{s}^{-1}\text{m}^{-2}\right]$ is the rate constant, $f_g(\text{Pa})$ is the fugacity of gaseous CO_2, and f_{eq} is the fugacity of the quadruple equilibrium. They obtained k_{D0} and ΔE for CO_2H as 1.83×10^8 mol $\text{Pa}^{-1}\text{s}^{-1}\text{m}^{-2}$ and 102.88 kJ mol^{-1}, respectively, at temperature and pressure

ranging from 274.15 to 281.15 K and from 1.4 to 3.3 MPa. However, new modified value of ΔE, if considered the real case in the ocean quoted from [16], is 96.49 kJ mol^{-1}. The order of Reynolds number based on the size of a particle, about 16 μm, is calculated as 50. Clarke et al. [28] determined the dissociation rate of CO2H by measuring the nucleated methane gas in V-L state [14]. The comparison of three models is listed in **Table 4**. The results of dissociation flux are summarized in **Figure 9**. Higher water temperature induces higher dissociation flux at the surface of hydrate. Data correlated by [14] show much lower level than both Nihous' model and new model. The numerical results in this work marked as new model in **Figure 9** show consistent result compared with Nihous' model. The dissociation flux in various flow rates in cases 5, 7, and 8 are listed in **Figure 10**. Here, it is noted that porosity is not considered in both Clarke's and Nihous' models, and these two models are only function of temperature and fugacity as presented in Eq. (15). The trend of flux becomes saturated in the figure due to the surface dissociation flux that becomes slow due to the fast mass transfer in bulk flow at Reynolds number over 100.

Item	Modeling	Intrinsic rate of dissociation	Ref.
Clarke's Model	Eq. (15)	K_{D0} = 1.83 * 10^8mole/Pa s m; ΔE = 102.89 kJ/mole	[14]
Nihous' Model	Eq. (15)	K_{D0} = 1.83 * 10^8mole/Pa s m; ΔE = 96.49 kJ/mole	[16]
New Model	Eq. (1)	K_{bl} = exp(−11,729/T + 26,398)	[21]

Table 4. The comparison of three models.

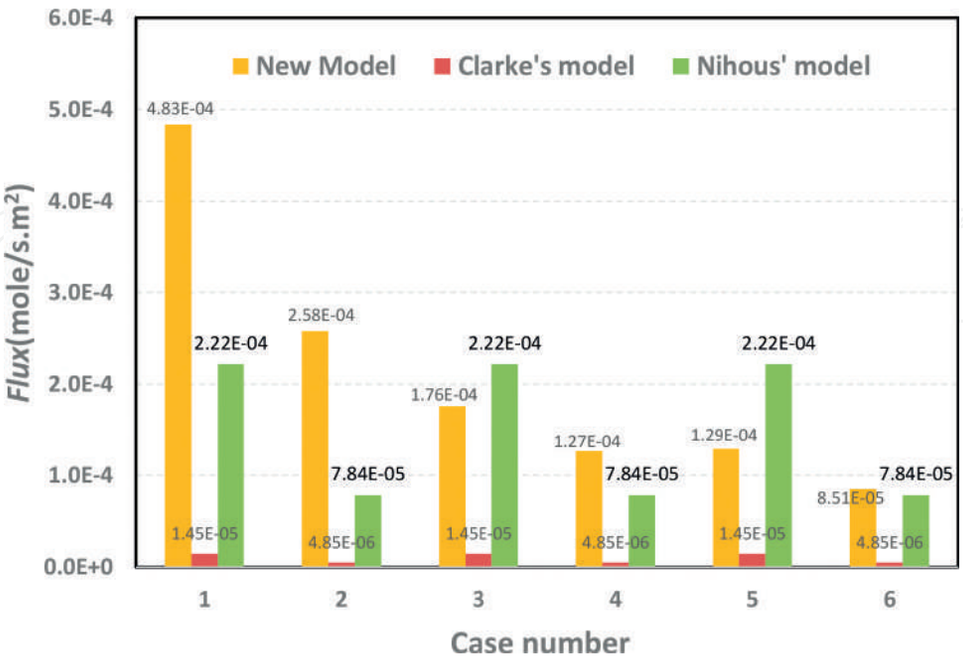

Figure 9. Results of simulation compared to existing two models.

http://dx.doi.org/10.5772/intechopen.74874

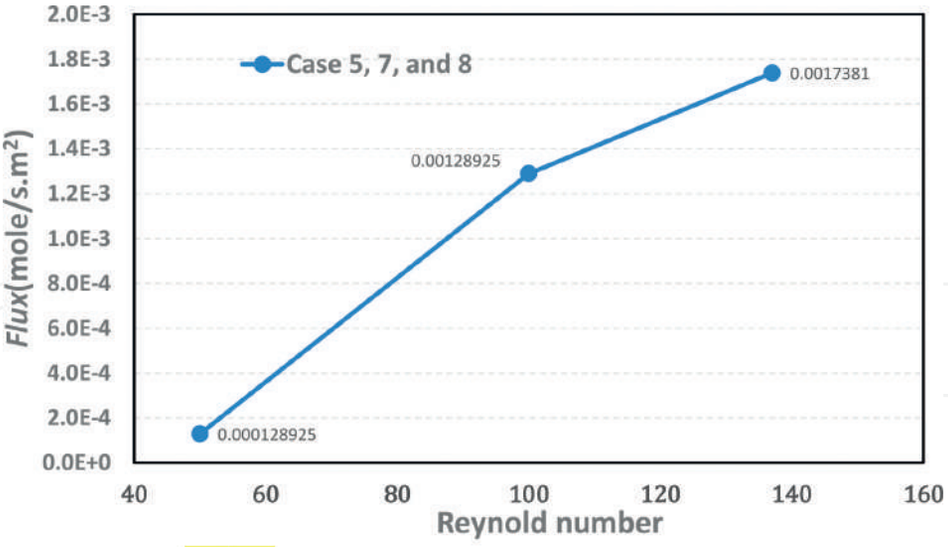

Figure 10. Results of flux in cases 5, 7, and 8.

10. Conclusions

The objective of this work is to establish a new pore-scale model for estimating the dissociation rate of CO_2H in laboratory-scale sediment samples. It is assumed that CO_2H formed homogeneously in spherical pellets. In the bulk flow, concentration and temperature of liquid CO_2 in water flow was analyzed by computational fluid dynamics (CFD) method without considering gas nucleation under high-pressure state. In this work, finite volume method (FVM) was applied in a face-centered regular packing in unstructured mesh. At the surface of hydrate, a dissociation model has been employed. Surface mass and heat transfer between hydrate and water are both visualized. The initial temperature 253.15 K of CO_2H pellets dissociated due to ambient warm water flow of 276.15 and 282.15 K and fugacity variation, ex. 2.01 and 1.23 MPa. Three tentative cases with porosity 74, 66, and 49% are individually simulated in this study. In the calculation, periodic conditions are imposed at each surface of packing. Additionally, the flux at CO_2H's surfaces is compared to Clarke and Bishnoi [13] and Nihous and Masutani [15] 's correlations at Reynolds number of 50. Numerical results of this work show good agreement with Nihous' model. Kinetic modeling by using 3D unstructured mesh of regular cubic unit and CFD scheme seems to be a simple tool to estimate the dissociation rate of CO_2H in laboratory-scale experiments, and could be easily extended to determine complex phenomena coupled with momentum, mass, and heat transfer in the sediment samples.

Acknowledgements

This work was supported by DOIT, Ministry of Science and Technology under contract No. MOST 106-3113-M-002-006. The authors also wish to acknowledge Professor Toru SATO for the valuable advices and guidance.

Nomenclature

C	volumetric molar concentration of CO_2 in the ambient water $\left[\text{mol m}^{-3}\right]$
C_H	volumetric molar concentration of CO_2 in the aqueous solution equilibrated with the stable hydrate phase $\left[\text{mol m}^{-3}\right]$
C'	volumetric molar concentration of CO_2 in water at the centroid of a cell attaching to the hydrate surface $\left[\text{mol m}^{-3}\right]$
C_I	volumetric molar concentration of CO_2 in the ambient aqueous solution at the surface of the hydrate ball $\left[\text{mol m}^{-3}\right]$
C_X	average molar volumetric concentration of CO_2 in the ambient water flow for a given cross section of water flow $\left[\text{mol m}^{-3}\right]$
d	diameter of the CO_2 hydrate ball [m]
D	diffusion coefficient of CO_2 in water $\left[\text{m s}^{-2}\right]$
E	activation energy $\left[\text{J mol}^{-1}\right]$
F	dissociation rate flux $\left[\text{mol s}^{-1}\ \text{m}^{-2}\right]$
f_{eq}	fugacity of the quadruple equilibrium [Pa].
f_g	fugacity of gaseous CO_2 [Pa]
G	molar Gibbs free energy $\left[\text{J mol}^{-1}\right]$
H_L	latent heat of hydrate dissociation $\left[\text{J mol}^{-1}\right]$
h_L	length of the water layer attached to the hydrate surface [m]
k_{D0}	intrinsic dissociate rate constant based on Clarke-Bishnoi model $\left[\text{mol Pa}^{-1}\text{s}^{-1}\text{m}^{-2}\right]$
k_{bl}	dissociation rate constant based on new model $\left[\text{mol}^2\ \text{J}^{-1}\ \text{s}^{-1}\text{m}^{-2}\right]$
L	thickness of computational cell [m]
M_B	molecular weight of water $\left[\text{g mol}^{-1}\right]$
P	thermodynamic pressure [Pa]
P_{eq}	quadruple equilibrium pressure for CO_2 hydrate as a function of T [Pa]
Q	volumetric flow rate of the ambient water $\left[\text{m}^3\text{s}^{-1}\right]$

http://dx.doi.org/10.5772/intechopen.74874

$\dot{Q}_H$	the rate at which the latent heat is transferred to the CO_2 hydrate by dissociation $\left[\mathrm{Jm^{-2}s^{-1}}\right]$
R	gas constant, 8.314 $\left[\mathrm{J\ K^{-1}\ mol^{-1}}\right]$
T	absolute temperature [K]
T_L	temperature at the centroids of a cell in the solid hydrate [K]
T_H	temperature at the centroids of a cell in the aqueous phase [K]
$\boldsymbol{u}$	velocity vectors [m/s]
x	mole fraction of CO_2 [-]
x_{eq}	solubility of CO_2 in the aqueous solution in equilibrium with the stable hydrate phase [-]
x_I	mole fraction of CO_2 in the aqueous phase at the surface of the hydrate ball [-]
α_L	thermal diffusivity in the aqueous phase $\left[\mathrm{m\ s^{-2}}\right]$
α_H	thermal diffusivity in the hydrate ball $\left[\mathrm{m\ s^{-2}}\right]$
Δr	thickness of the computational cell [m]
δ	thickness of the boundary layer [m]
$\Delta\mu$	chemical potential difference $\left[\mathrm{J\ mol^{-1}}\right]$
ρ_w	density of the ambient water $\left[\mathrm{kg\ m^{-3}}\right]$
φ	the association parameter for the solvent water
η_L	the viscosity of water [mPa s]
V_A	the molar volume of CO_2 $\left[\mathrm{m^3mol^{-1}}\right]$
ν_L	kinematic viscosity of water $\left[\mathrm{ms^{-2}}\right]$
λ_L	heat conductivity of water $\left[\mathrm{W\ K^{-1}\ m^{-1}}\right]$
λ_H and λ_L	the heat conductivities in the hydrate and water $\left[\mathrm{WK^{-1}m^{-1}}\right]$

Author details

Wu-Yang Sean

Address all correspondence to: wuyangsean@gmail.com

Department of Environmental Engineering, Chung Yuan Christian University, Taiwan

References

[1] Jeong S-M, Hsieh L-HC, Huang C-Y, Sean W-Y. Direct numerical simulation of CO_2 hydrate dissociation in pore-scale flow by applying CFD method. International Journal of Heat and Mass Transfer. 2017;**107**:300-306

[2] Andersson V, Kvaerner A, Haines M. Gas hydrates for deep ocean storage of CO_2—novel technology for utilising hydrates for transport of CO_2. In: Wilson M, Morris T, Gale J, Thambimuthu K, editors. Greenhouse Gas Control Technologies, Volume II. New York: Elsevier; 2005. pp. 1487-1492

[3] Molins S, Trebotich D, Steefel CI, Shen C. An investigation of the effect of pore scale flow on average geochemical reaction rates using direct numerical simulation. Water Resources Research. 2012;**48**:7453-7460. DOI: 10.1029/2011WR011404

[4] Davison SM, Yoon H, Martinez MJ. Pore scale analysis of the impact of mixing-induced reaction dependent viscosity variations. US Department of Energy Publications. Paper 110. 2012. http://digitalcommons.unl.edu/usdoepub/110

[5] Gregor R, Stephen HK, William BD, Laura AS, Edward TP, John P, Peter GB. Dissolution rates of pure methane hydrate and carbon-dioxide hydrate in undersaturated seawater at 1000-m depth. Geochimica et Cosmochimica Acta. 2004;**68**(2):285-292

[6] Inui M, Sato T. Economical feasibility study on CO_2 sequestration in the form of hydrate under seafloor. Proceedings of 26th International Conference on Offshore Mechanical and Arctic Engineering. 2006;OMAE06-92306:1-10

[7] Uchida T, Ebinuma T, Takeya S, Nagao J, Narita H. Effects of pore sizes on dissociation temperatures and pressures of methane, carbon dioxide, and propane hydrates in porous media. The Journal of Physical Chemistry. B. 2002;**106**:820-826

[8] Jung RT, Sato T. Numerical simulation of high Schmidt number flow on unstructured hybrid mesh. Journal of Computational Physics. 2004;**203**:221-249

[9] Sloan ED. Clathrate hydrate of natural gases. New York: Dekker; 1998

[10] Aya I, Yamane K, Nariai H. Solubility of CO_2 and density of CO_2 hydrate at 30MPa. Energy. 1997;**22**:263-271

[11] Yang SO, Yang IM, Kim YS, Lee CS. Measurement and prediction of phase equilibria for water + CO_2 in hydrate forming condition. Fluid Phase Equilibria. 2000;**175**:75-89

[12] Servio P, Englezos P. Effect of temperature and pressure on the solubility of carbon dioxide in water in the presence of gas hydrate. Fluid Phase Equilibria. 2001;**190**:127-134

[13] Clarke MA, Bishnoi PR. Determination of the intrinsic rate constant and activation energy of CO_2 gas hydrate decomposition using in-situ particle size analysis. Chemical Engineering Science. 2004;**59**:2983-2993

[14] Sean W, Sato T, Yamasaki A, Kiyono F. CFD and experimental study on methane hydrate dissociation part II. General cases. AICHE Journal. 2007;**53**:2148-2160

[15] Nihous GC, Masutani SM. Notes on the dissolution rate of gas hydrates in undersaturated water. Chemical Engineering Science. 2006;**61**:7827-7830

[16] O'Connor RM, Fredrich JT. Microscale flow modelling in geologic materials. Physics and Chemistry of the Earth, Part A: Solid Earth and Geodesy. 1999;**24**(7):611-616

[17] Piller M, Nolich M, Favretto S, Radaelli F, Rossi E. Analysis of hydraulic permeability in porous media: From high resolution X-ray tomography to direct numerical simulation. Transport in Porous Media. 2009;**80**(1):57-78

[18] Sahimi M. Flow and Transport in Porous Media and Fractured Rock. Weinheim: VCG; 1995

[19] Boomsma K, Poulikakos D, Ventikos Y. International Journal of Heat and Fluid Flow. 2003;**24**:825

[20] Fukumoto A, Sean WY, Sato T, Yamasaki A, Kiyono F. Estimation of dissociation rate constant of CO_2 hydrate in water flow. Greenhouse Gases: Science and Technology. 2015; **5**(2):169-179

[21] Pohlhausen E. Der Wärmeaustausch zwischen festen Körpern und Flüssigkeiten mit kleiner reibung und kleiner Wärmeleitung. Zeitschrift für Angewandte Mathematik und Mechanik. 1921;**1**:115-121. DOI: 10.1002/zamm.19210010205

[22] Shu SS, Lee MJ. Dynamic behavior of methane hydrates formation and decomposition with a visual high-pressure apparatus. Journal of the Taiwan Institute of Chemical Engineers. 2016;**62**:1-9

IntechOpen

IntechOpen

IntechOpen

We are IntechOpen, the world's leading publisher of Open Access books
Built by scientists, for scientists

6,300
Open access books available

171,000
International authors and editors

190M
Downloads

Our authors are among the

154
Countries delivered to

TOP 1%
most cited scientists

12.2%
Contributors from top 500 universities

CLARIVATE ANALYTICS
BOOK CITATION INDEX
INDEXED

WEB OF SCIENCE™

Selection of our books indexed in the Book Citation Index in Web of Science™ Core Collection (BKCI)

Interested in publishing with us?
Contact book.department@intechopen.com

Numbers displayed above are based on latest data collected.
For more information visit www.intechopen.com

Chapter 3

Darcy-Forchheimer Flow of Casson Nanofluid with Heat Source/Sink: A Three-Dimensional Study

Gosikere Kenchappa Ramesh

Additional information is available at the end of the chapter

http://dx.doi.org/10.5772/intechopen.74170

Abstract

In this chapter, three-dimensional Casson nanoliquid flow in two lateral directions past a porous space by Darcy-Forchheimer articulation is examined. The study includes the impact of uniform heat source/sink and convective boundary condition. The administering partial differential equations are shaped to utilizing comparability changes into a set of nonlinear normal differential conditions which are fathomed numerically. The self-comparative arrangements are gotten and contrasted and accessible information for uncommon cases. The conduct of parameters is displayed graphically and examined for velocity, temperature, and nanoparticle volume part. It is discovered that temperature and nanoparticle volume fraction rise for enhancement of Forchheimer and porosity parameters.

Keywords: three-dimensional flow, Darcy-Forchheimer porous medium, Casson nanoliquid, uniform heat source/sink, convective boundary condition, numerical solutions

1. Introduction

In many assembling processes and for mechanical reason, the investigation of heat exchange and boundary layer flow over linearly and nonlinearly extending surface are much imperative. These procedures and applications incorporate streamlined feature forming, wire drawing, and paper generation where a specific temperature will be required for cooling the particles in the liquid. At first, the stream qualities have been analyzed by [1] overextending surfaces. The perfection of finishing up item relies upon the rate of warmth exchange at the surface of extending material. Many creators expanded crafted by [1] managed heat exchange qualities alongside the flow conduct in different physical circumstances in [2–8].

IntechOpen

© 2018 The Author(s). Licensee IntechOpen. This chapter is distributed under the terms of the Creative Commons Attribution License (http://creativecommons.org/licenses/by/3.0), which permits unrestricted use, distribution, and reproduction in any medium, provided the original work is properly cited. CC BY

Non-Newtonian fluids can't be portrayed because of nonexistence of single constitutive connection among stress and rate of strain. In the current year, non-Newtonian fluids have turned out to be increasingly essential because of its mechanical applications. Truth be told, the enthusiasm for boundary layer flows of non-Newtonian fluid is expanding significantly because of its extensive number of functional applications in industry producing preparing and natural fluids. Maybe, a couple of principle illustrations identified with applications are plastic polymer, boring mud, optical fibers, paper generation, hot moving, metal turning, and cooling of metallic plates in a cooling shower and numerous others. Since no single non-Newtonian model predicts every one of the properties of non-Newtonian fluid along these lines examinations proposed different non-Newtonian fluid models. These models are essentially classified into three classifications specifically differential-, rate-, and fundamental-type fluids. In non-Newtonian fluid, shear stresses and rates of strain/disfigurement are not directly related. Such fluid underthought which does not comply with Newton's law is a straightforward non-Newtonian fluid model of respectful sort. In 1959, Casson displayed this model for the flow of viscoelastic fluids. This model has a more slow progress from Newtonian to the yield locale. This model is utilized by oil builds in the portrayal of bond slurry and is better to predict high shear-rate viscosities when just low and middle road shear-rate information are accessible. The Casson show is more exact at both high and low shear rates. Casson liquid has one of the kind attributes, which have wide application in sustenance handling, in metallurgy, in penetrating operation and bio-designing operations, and so on. The Casson show has been utilized as a part of different businesses to give more exact portrayal of high shear-rate viscosities when just low and moderate shear-rate information are accessible [9]. Toward the starting Nadeem et al. [10] introduce the idea of Casson fluid and demonstrate over an exponentially extending sheet. Numerous examinations identified with viscoelastic properties of liquid are underthought [11–17].

The nanoparticles in by and large are made of metal oxides, metallic, carbon, or some other materials [18]. Standard fluid has weaker conductivity. This weaker conductivity can be enhanced incredibly with the utilization of nanoparticles. Truly, the Brownian movement factor of nanoparticles is base fluid and is essential toward this path. An extraordinary measure of warmth is delivered in warm exchangers and microelectromechanical procedures to lessen the framework execution. Fluid thermal conductivity is enhanced by nanoparticle expansion just to cool such modern procedures. The nanoparticles have shallow significance in natural and building applications like prescription, turbine sharp-edge cooling, plasma- and laser-cutting procedure, and so on. Sizeable examinations on nanofluids have been tended to in the writing. Buongiorno [19] has investigated the mechanisms of nanofluid by means of snapshot of nanoparticles in customary base fluid. Such instruments incorporate nanoparticle measure, Magnus effect, dormancy, molecule agglomeration, Brownian movement, thermophoresis, and volume portion. Here, we introduce some imperative scientists who have been accounted for by considering the highlights of thermophoretic and Brownian movement [20–27].

In displaying the flow in permeable media, Darcy's law is a standout among the most prominent models. Particularly, flow in permeable media is exceptionally valuable in grain stockpiling, development of water in repositories, frameworks of groundwater, fermentation process, raw petroleum generation, and oil assets. In any case, it is by and large

perceived that Darcy's model may over anticipate the convective streams when the inertial drag and vorticity dissemination coproductive are considered. The expansion of established Darcy demonstrates incorporates inertial drag and vorticity dispersion. To think about the inertial drag and vorticity dispersion, Forchheimer [28] joined the root mean square. Forchheimer's term was named by Muskat [29] and inferred that the consideration of Forchheimer's term is substantial for high Reynolds number. Pal and Mondal [30] examined the hydromagnetic Darcy-Forchheimer flow for variable liquid property. Utilizing HAM strategy, Hayat et al. [31] got the systematic answer for Darcy-Forchheimer stream of Maxwell liquid by considering the Cattaneo-Christov hypothesis. Vishnu Ganesh et al. [32] analyzed the thick and Ohmic dispersals, and the second-order slip consequences for Darcy-Forchheimer flow of nanoliquid past an extending/contracting surface. Scientific model for Darcy-Forchheimer stream of Maxwell fluid with attractive field and convective boundary condition is given by Sadiq and Hayat [33]. Utilizing Keller's box strategy, Ishak et al. [34] numerically examined the magnetohydrodynamic flow and heat exchange exhibitions over an extending cylinder. Mixed convective flow and the related warmth and mass exchange qualities over a vertical sheet immersed in a permeable medium have been explored by Pal and Mondal [35] by considering different impacts, for example, Soret, Dufour, and thermal radiation.

The principle objective here is to uncover the Darcy-Forchheimer connection on a three-dimensional Casson nanofluid flow past a stretching sheet. Heat transfer is handled with regular heat generation/absorption and convective-type boundary condition.

2. Mathematical formulation

Three-dimensional flow of Casson nanofluid filling permeable space by Darcy-Forchheimer connection is considered. Flow is bidirectional extending surface. Nanofluid model depicts the properties of Brownian dispersion and thermophoresis. Concurrent states of heat convective and heat source/sink are executed. We receive the Cartesian coordinate in such a way to the point that and pivot are picked along x and y ordinary to the stretchable surface. Let $U_w(x) = ax$ and $V_w(y) = by$ be the extending velocity along x and y directions separately. The surface temperature is directed by a convective heating procedure which is depicted by heat exchange coefficient h_f and temperature of hot liquid T_f under the surface (see **Figure 1**). The boundary layer equations for flow underthought are

$$\frac{\partial u}{\partial x}+\frac{\partial v}{\partial y}+\frac{\partial w}{\partial z} = 0, \tag{1}$$

$$u\frac{\partial u}{\partial x}+v\frac{\partial u}{\partial y}+w\frac{\partial u}{\partial z} = \nu\left(1+\frac{1}{\beta}\right)\frac{\partial^2 u}{\partial z^2}-\frac{\nu}{K}u-Fu^2, \tag{2}$$

$$u\frac{\partial v}{\partial x}+v\frac{\partial v}{\partial y}+w\frac{\partial v}{\partial z} = \nu\left(1+\frac{1}{\beta}\right)\frac{\partial^2 v}{\partial z^2}-\frac{\nu}{K}v-Fv^2, \tag{3}$$

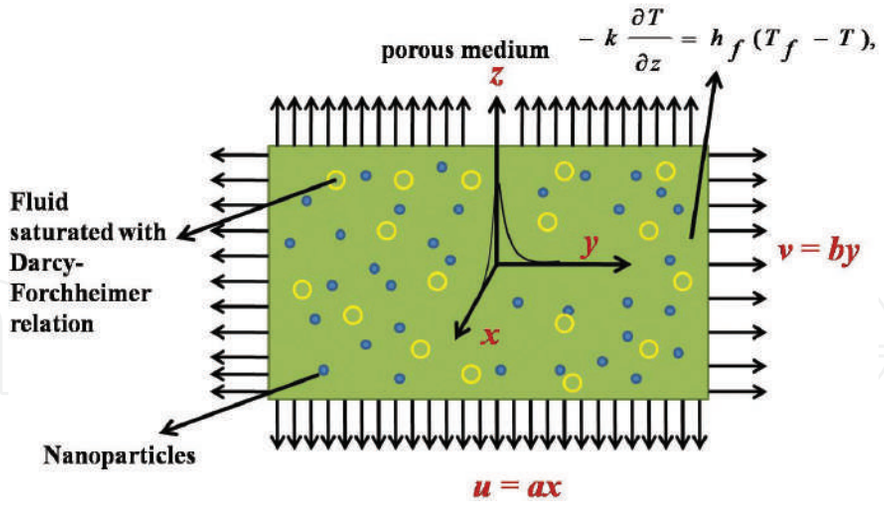

Figure 1. Geometry of the problem.

$$u\frac{\partial T}{\partial x} + v\frac{\partial T}{\partial y} + w\frac{\partial T}{\partial z} = \alpha_m\frac{\partial^2 T}{\partial z^2} + \frac{(\rho c)_p}{(\rho c)_f}\left(D_B\left(\frac{\partial T}{\partial z}\frac{\partial C}{\partial z}\right) + \frac{D_T}{T_\infty}\left(\frac{\partial T}{\partial z}\right)^2\right) + \frac{q_0}{(\rho c)_p}(T - T_\infty) \tag{4}$$

$$u\frac{\partial C}{\partial x} + v\frac{\partial C}{\partial y} + w\frac{\partial C}{\partial z} = D_B\left(\frac{\partial^2 C}{\partial z^2}\right) + \frac{D_T}{T_\infty}\left(\frac{\partial^2 T}{\partial z^2}\right) \tag{5}$$

and boundary conditions of the problem is

$$u = ax, v = by, w = 0, -k\frac{\partial T}{\partial z} = h_f(T_f - T), C = C_w \text{ at } z = 0$$

$$u \to 0, v \to 0, T \to T_\infty, C \to C_\infty \text{ as } z \to \infty \tag{6}$$

Here u, v and w represent as components of velocity in x, y and z directions, respectively; $\nu = \frac{\mu}{\rho_f}$ stands for kinematic viscosity; μ for dynamic viscosity; ρ_f for density of base liquid; K for permeability of porous medium; $F = \frac{C_b}{xK^{\frac{1}{2}}}$ for nonuniform inertia coefficient of porous medium; C_b for drag coefficient; T for temperature; $\alpha_m = \frac{K}{(\rho c)_f}$ for thermal diffusivity; q_0 volumetric rate of heat generation and absorption; β is the Casson parameter; k for thermal conductivity; $(\rho c)_p$ for effective heat capacity of nanoparticles; $(\rho c)_f$ for heat capacity of fluid; C for concentration; D_B for Brownian diffusion coefficient; D_T for thermophoretic diffusion coefficient; T_∞ for ambient fluid temperature; C_∞ for ambient fluid concentration; and a and b for positive constants.

Selecting similarity transformations are

$$u = axf'(\varsigma), v = ayg'(\varsigma), w = -(a\nu)^{\frac{1}{2}}(f + g),$$

$$\theta(\varsigma) = \frac{T - T_\infty}{T_f - T_\infty}, \phi(\varsigma) = \frac{C - C_\infty}{C_w - C_\infty}, \varsigma = \left(\frac{a}{\nu}\right)^{\frac{1}{2}} z \tag{7}$$

Applying Eq. (7) in (1) is verified. and Eqs. (2)–(5) are

$$\left(1 + \frac{1}{\beta}\right) f''' + (f + g) f'' - f'^2 - \lambda f' - F_r f'^2 = 0 \tag{8}$$

$$\left(1 + \frac{1}{\beta}\right) g''' + (f + g) g'' - g'^2 - \lambda g' - F_r g'^2 = 0 \tag{9}$$

$$\theta'' + \Pr\left((f + g)\theta' + Nb\theta'\phi' + Nt\theta'^2\right) + \Pr Q\theta(\eta) = 0 \tag{10}$$

$$\phi'' + Le \Pr(f + g)\phi' + \frac{Nt}{Nb}\theta'' = 0 \tag{11}$$

Boundary conditions of Eq. (6) become

$$f(0) = g(0) = 0,\ f'(0) = 1,\ g'(0) = \alpha,\ \theta'(0) = -Bi(1 - \theta(0)), \phi(0) = 1,$$

$$f'(\infty) \to 0,\ g'(\infty) \to 0,\ \theta(\infty) \to 0, \phi(\infty) \to 0 \tag{12}$$

In the above expressions, λ stands for porosity parameter, F_r for Forchheimer parameter, α for ratio parameter, Pr for Prandtl number, Le for Schmidt number, Bi for Biot number, Nt for thermophoresis parameter, Nb for Brownian motion parameter, and Q heat source/sink parameter.

These dimensionless variables are given by

$$\lambda = \frac{\nu}{Ka}, F_r = \frac{C_b}{K^{\frac{1}{2}}}, \alpha = \frac{b}{a}, \Pr = \frac{\nu}{\alpha_m}, Le = \frac{\nu}{D_B}, Q = \frac{q_0}{a\rho c_p}, Bi = \frac{h_f}{k}\sqrt{\frac{\nu}{a}},$$

$$Nt = \frac{(\rho c)_p D_T (T_f - T_\infty)}{(\rho c)_f \nu T_\infty}, Nb = \frac{(\rho c)_p D_B C_\infty}{(\rho c)_f \nu}.$$

Dimensionless relations of skin friction coefficient, local Nusselt number, and local Sherwood number are as follows:

$$\mathrm{Re}_x^{\frac{1}{2}} C_{fx} = \left(1 + \frac{1}{\beta}\right) f''(0), \left(\frac{x}{y}\right) \mathrm{Re}_y^{\frac{1}{2}} C_{fy} = \alpha\left(1 + \frac{1}{\beta}\right) g''(0),$$

$$\mathrm{Re}_x^{-\frac{1}{2}} N u_x = -\theta'(0), \text{ and } \mathrm{Re}_x^{-\frac{1}{2}} S u_x = -\phi'(0),$$

where $\mathrm{Re}_x = U_w \frac{x}{\nu}$ and $\mathrm{Re}_y = V_w \frac{y}{\nu}$ depict the local Reynolds numbers.

3. Results and discussion

The correct arrangements do not appear to be achievable for an entire arrangement of Eqs. (8)–(11) with proper limit conditions given in Eq. (12) in light of the nonlinear shape. This reality compels one to get the arrangement of the issue numerically. Suitable likeness change is received to change the overseeing incomplete differential conditions into an arrangement of non-straight customary differential conditions. The resultant limit esteem issue is understood numerically utilizing an efficient fourth-order Runge-Kutta method alongside shooting method (see Ramesh and Gireesha [27]). Facilitate the union examination is available in **Table 1**. For the verification of precision of the connected numerical plan, an examination of the present outcomes compared to the $-\left(1+\frac{1}{\beta}\right)f''(0)$ and $-\left(1+\frac{1}{\beta}\right)g''(0)$ (nonappearance of Forchheimer parameter, porosity parameter) with the accessible distributed consequences of Ahmad and Nazar [16] and Nadeem et al. [15] is made and exhibited in **Table 2**, demonstrates a great understanding in this manner give confidence that the numerical outcomes got are precise.

This section is fundamentally arranged to depict the effect of different correlated physical parameters on velocity profiles $f'(\varsigma)$, $g'(\varsigma)$, temperature profile $\theta(\varsigma)$, nanoparticle part $\phi(\varsigma)$, skin

ς	$f(\varsigma)$	$f'(\varsigma)$	$-f''(\varsigma)$
0	0.000000	1.000000	0.763674
1	0.695167	0.456344	0.365768
2	1.008110	0.202536	0.166242
3	1.146071	0.088680	0.073585
4	1.206291	0.038589	0.032175
5	1.232460	0.016746	0.013992
6	1.243809	0.007258	0.006070
7	1.248727	0.003144	0.002630
8	1.250857	0.001362	0.001139
9	1.251780	0.000590	0.000493
10	1.252179	0.000255	0.000213
11	1.252352	0.000111	0.000092
12	1.252427	0.000047	0.000040
13	1.252460	0.000020	0.000017
14	1.252474	0.000008	0.000007
15	1.252480	0.000006	0.000003
16	1.252482	0.000001	0.000001
17	1.252483	0.000000	0.000000

Table 1. Convergence analysis of the present work.

β	$c = 0$	$c = 0.5$		$c = 1.0$
	$-\left(1+\frac{1}{\beta}\right)f''(0)$	$-\left(1+\frac{1}{\beta}\right)f''(0)$	$-\left(1+\frac{1}{\beta}\right)g''(0)$	$-\left(1+\frac{1}{\beta}\right)g''(0)$
1	1.414213	1.545869	0.657899	1.659891
	[15, 16]	[15, 16]	[15, 16]	[15, 16]
5	1.095445	1.197425	0.509606	1.285746
	[15, 16]	[15, 16]	[15, 16]	[15, 16]
1000	1.000499	1.093641	0.465437	1.174307
	[15, 16]	[15, 16]	[15, 16]	[15, 16]

Table 2. Current numerical values and validation for friction factor $-\left(1+\frac{1}{\beta}\right)f''(0)$.

friction coefficient, and the local Nusselt and local Sherwood number through **Figures 2–16**. Give the first focus on the impact of extending parameter (α) on velocity profile as shown in **Figure 2**. It is noticed that for expanding benefits of extending parameter α, it decreases the speed $f'(\varsigma)$, while $g'(\varsigma)$ fluctuates for different benefits of extending parameter α. It see that for $\alpha = 0$, exhibit wonders lessen the instance of two dimensional linear stretching, while for

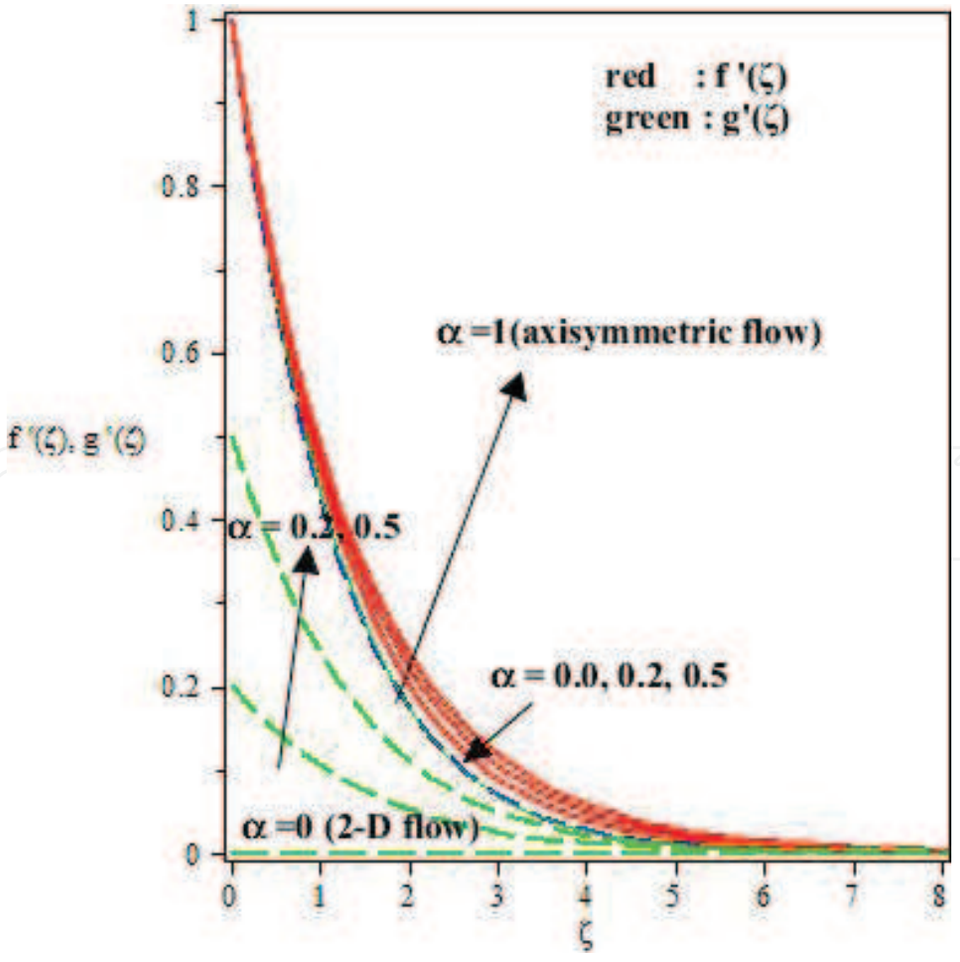

Figure 2. Influence of α on velocity field.

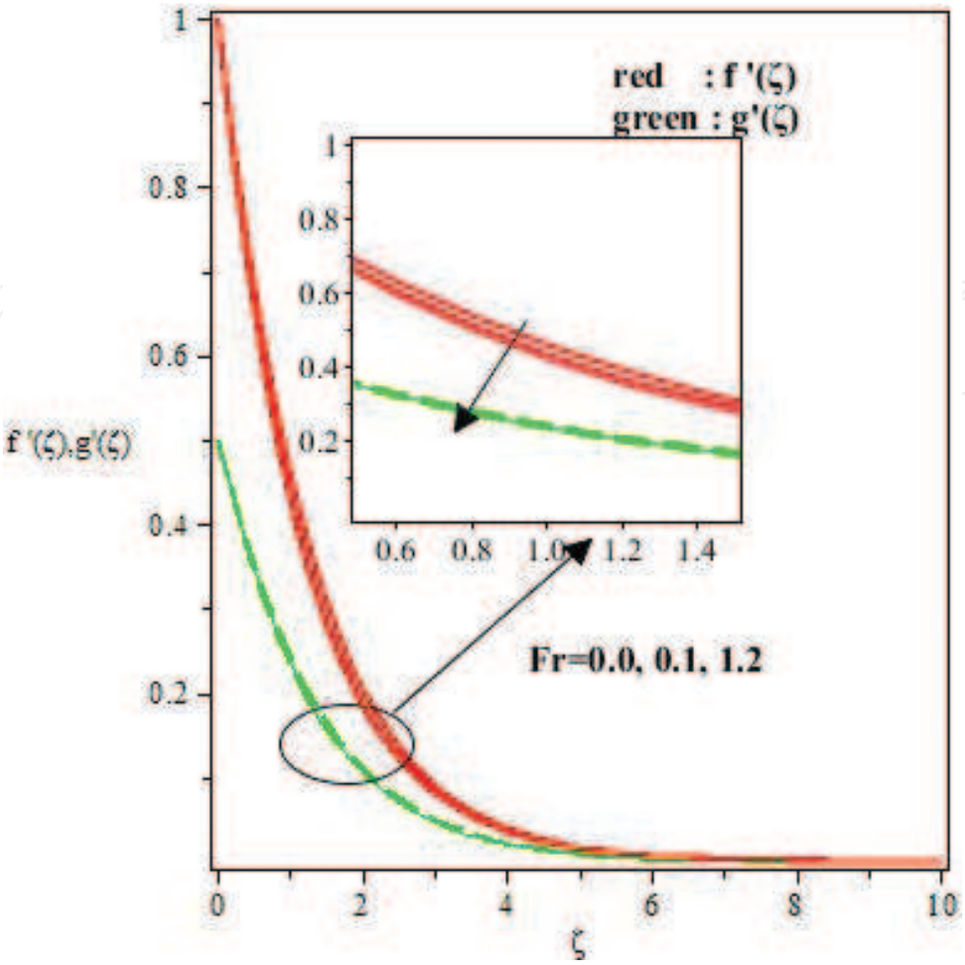

Figure 3. Influence of *Fr* on velocity fields.

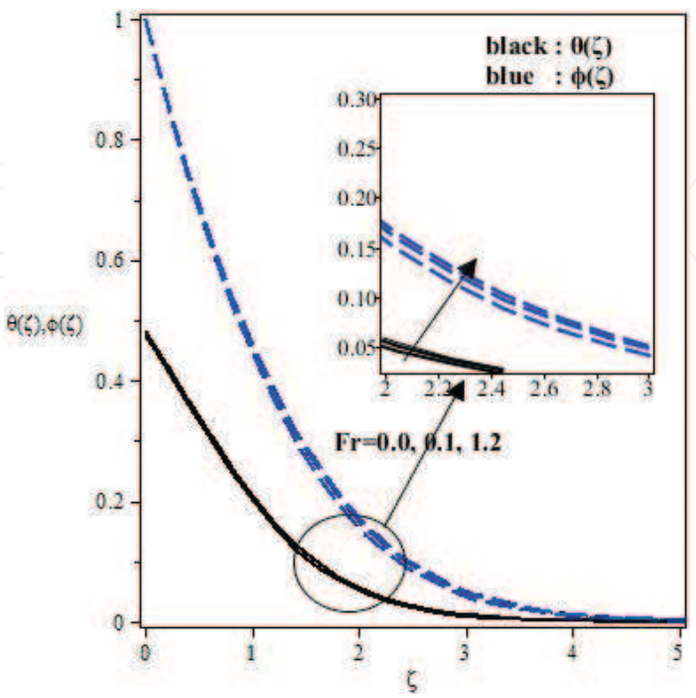

Figure 4. Influence of *Fr* on temperature and concentration fields.

http://dx.doi.org/10.5772/intechopen.74170

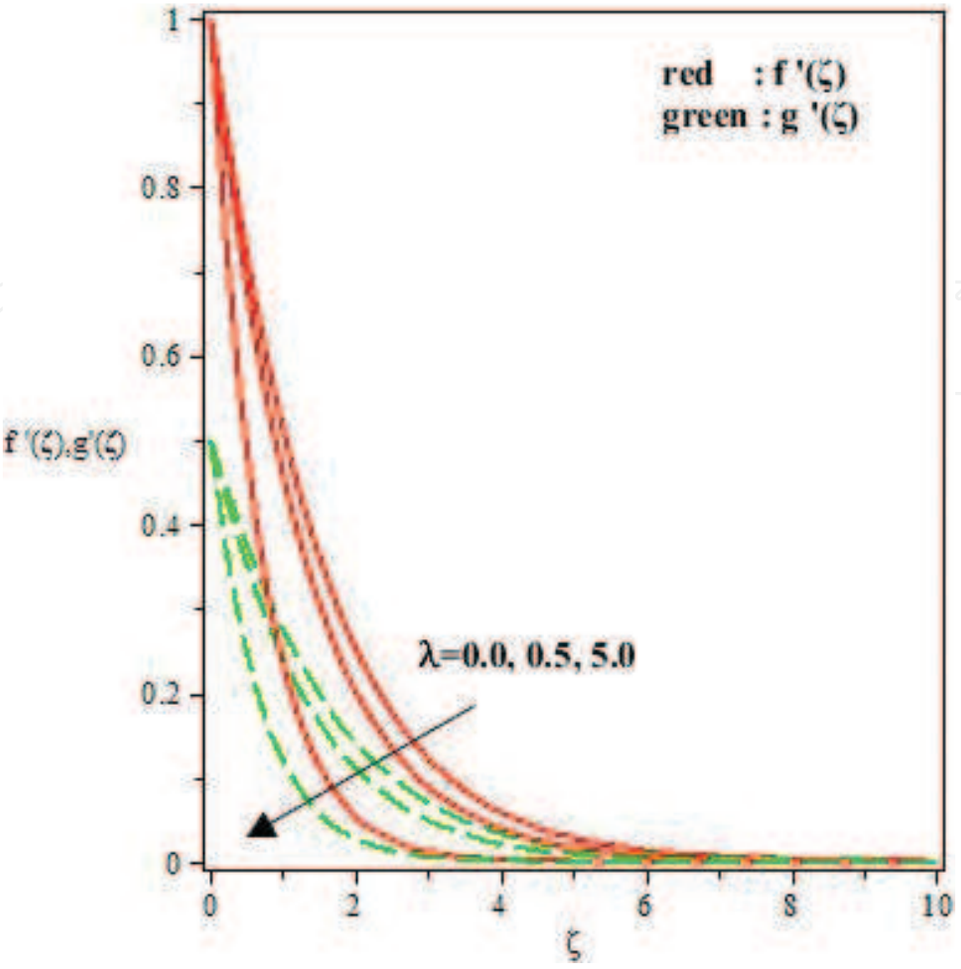

Figure 5. Influence of λ on velocity field.

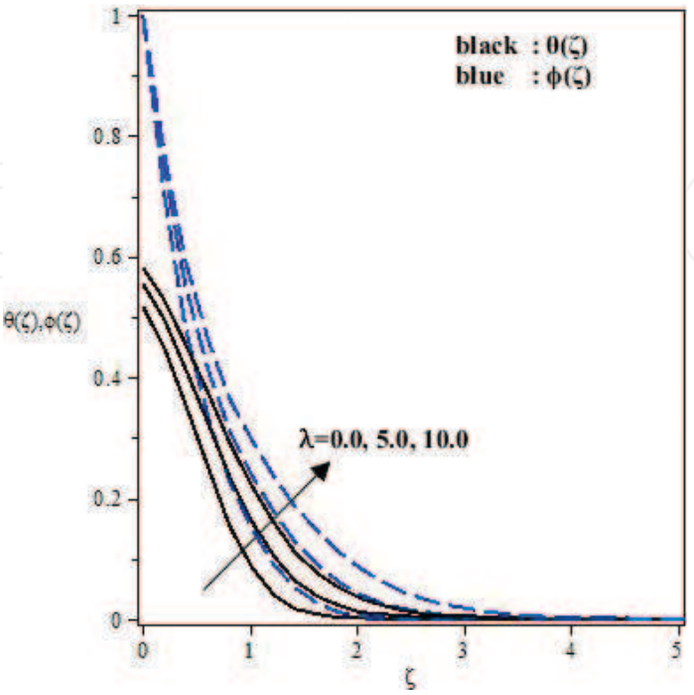

Figure 6. Influence of λ on temperature and concentration fields.

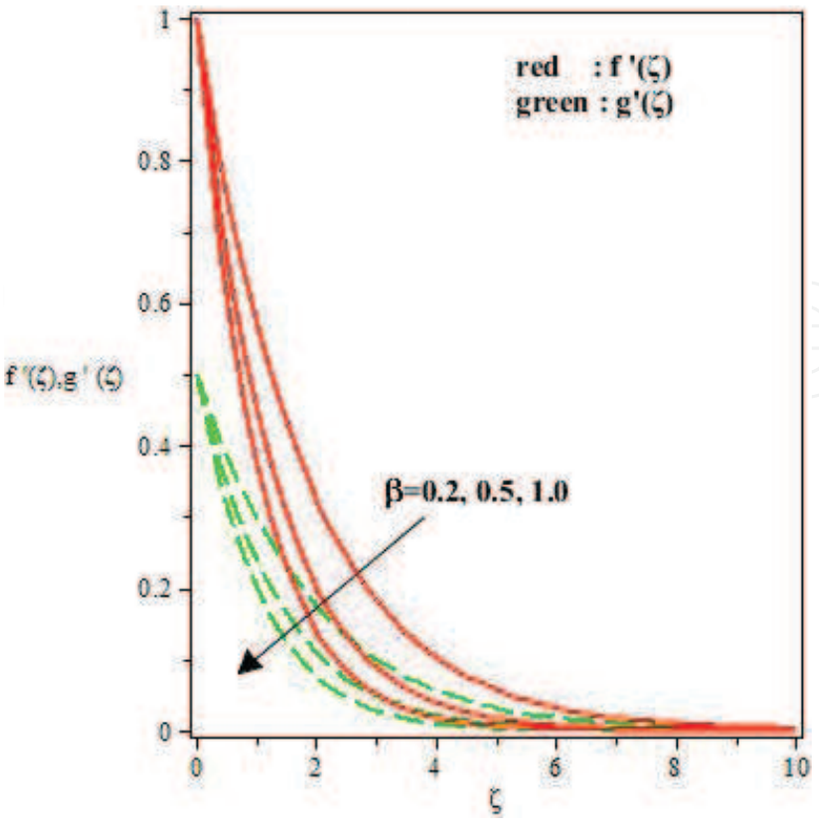

Figure 7. Influence of β on velocity fields.

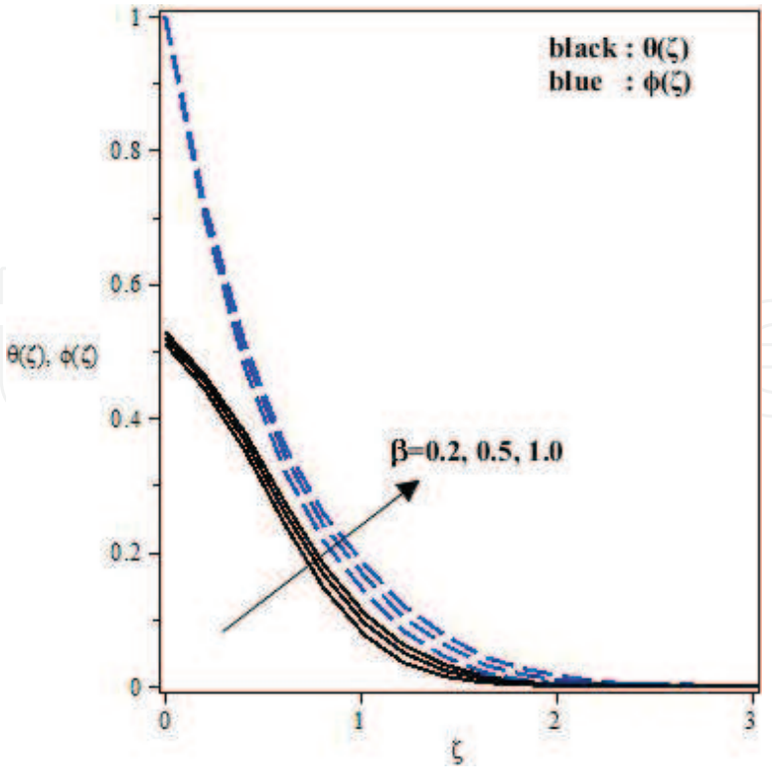

Figure 8. Influence of β on temperature and concentration fields.

http://dx.doi.org/10.5772/intechopen.74170

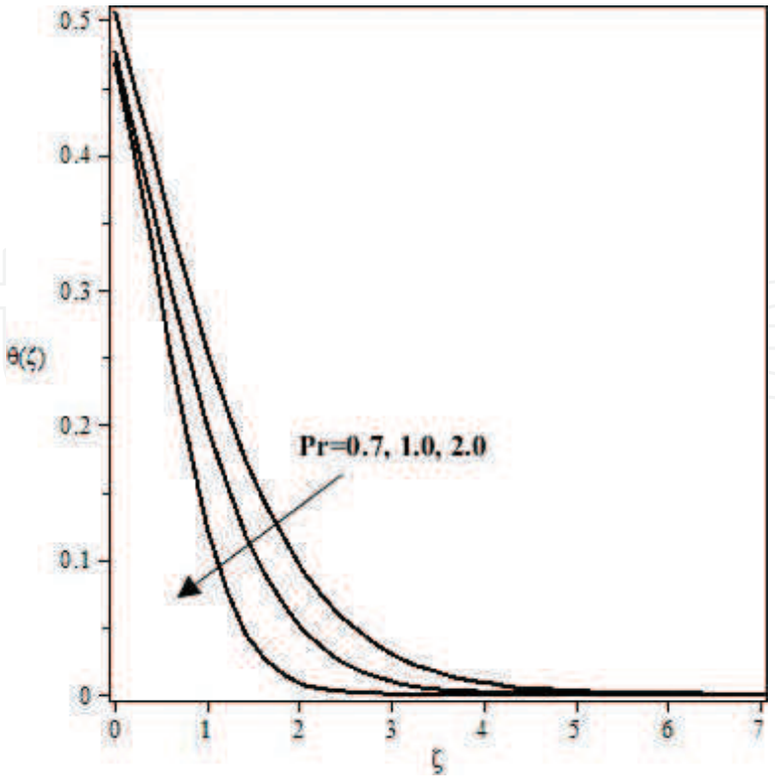

Figure 9. Influence of Pr on temperature fields.

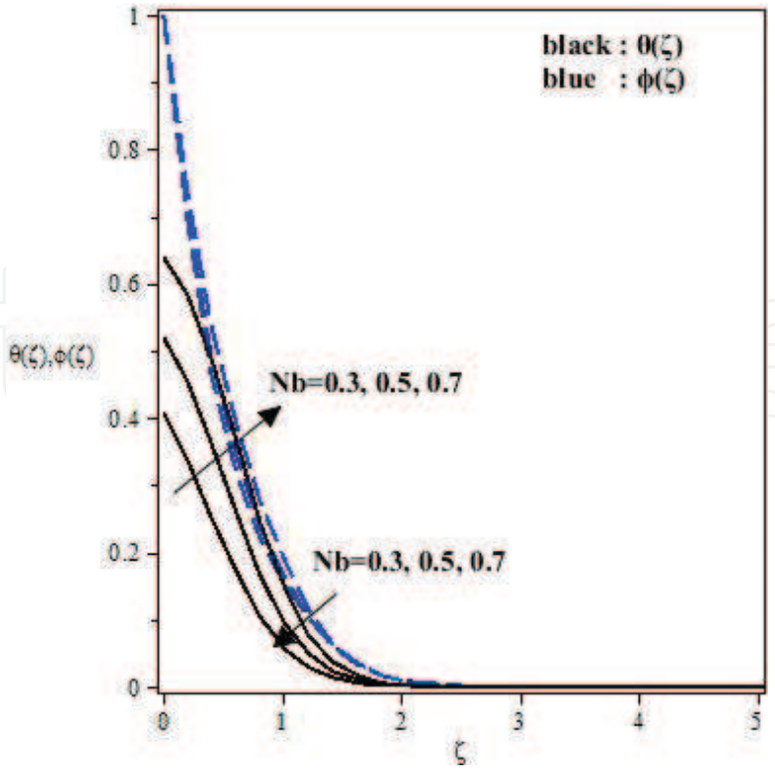

Figure 10. Influence of *Nb* on temperature and concentration fields.

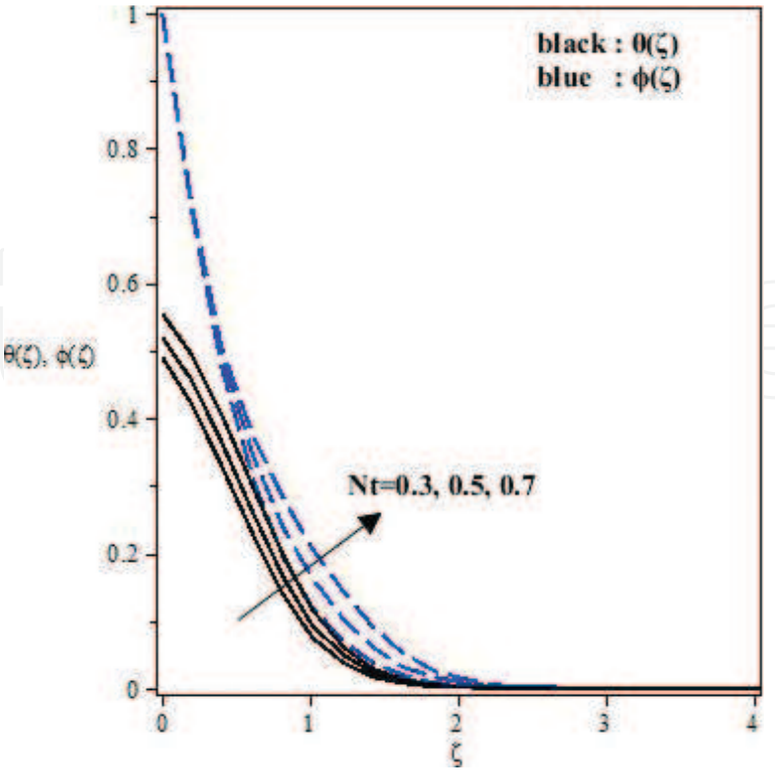

Figure 11. Influence of *Nt* on temperature and concentration fields.

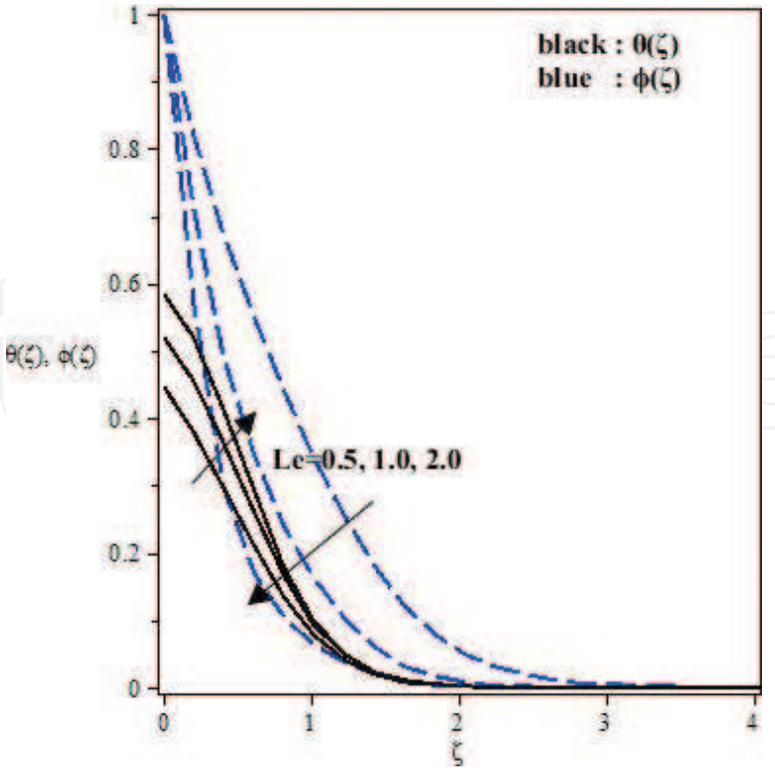

Figure 12. Influence of *Le* on temperature and concentration fields.

http://dx.doi.org/10.5772/intechopen.74170

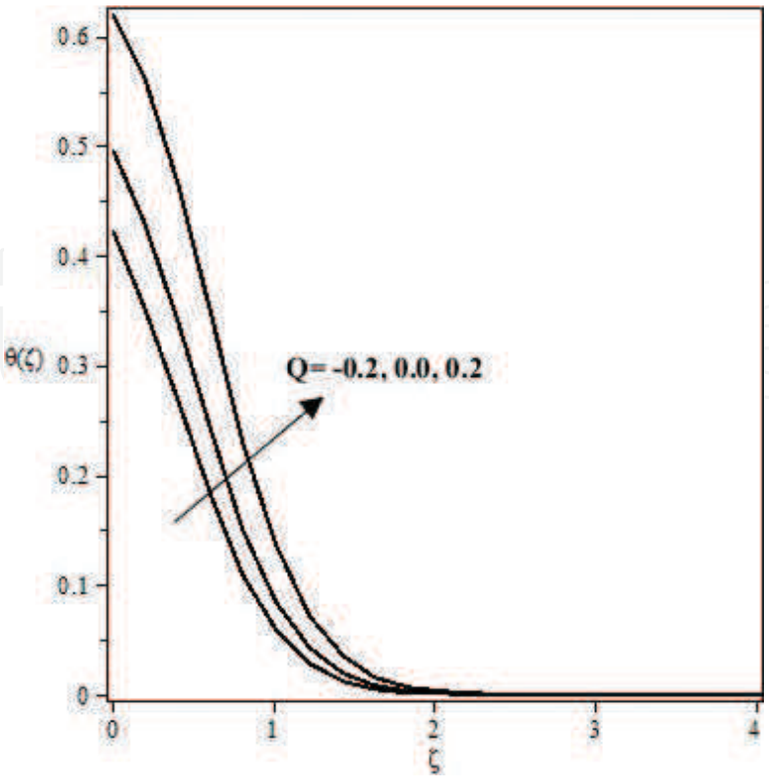

Figure 13. Influence of Q on temperature field.

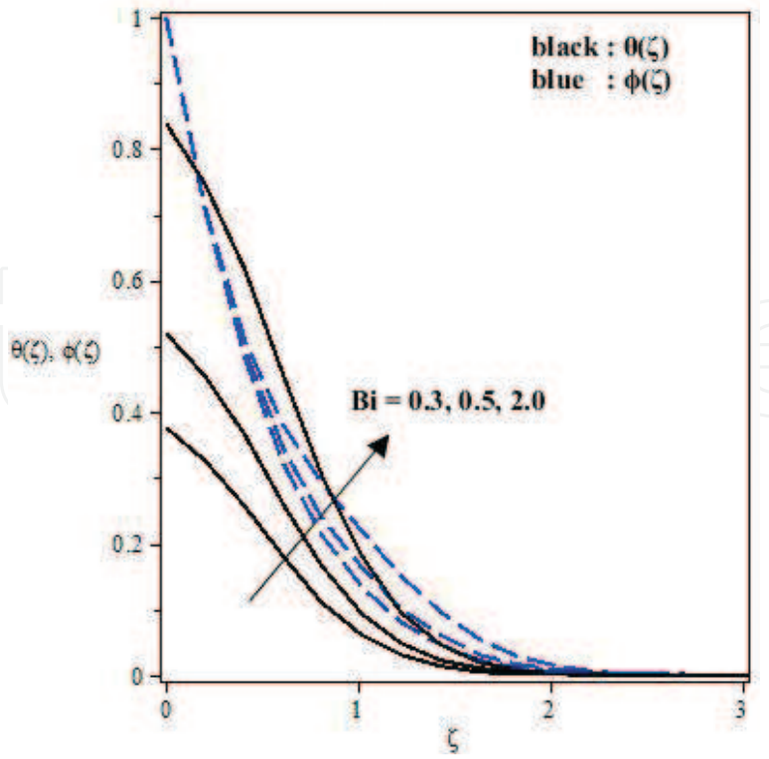

Figure 14. Influence of Bi on temperature and concentration fields.

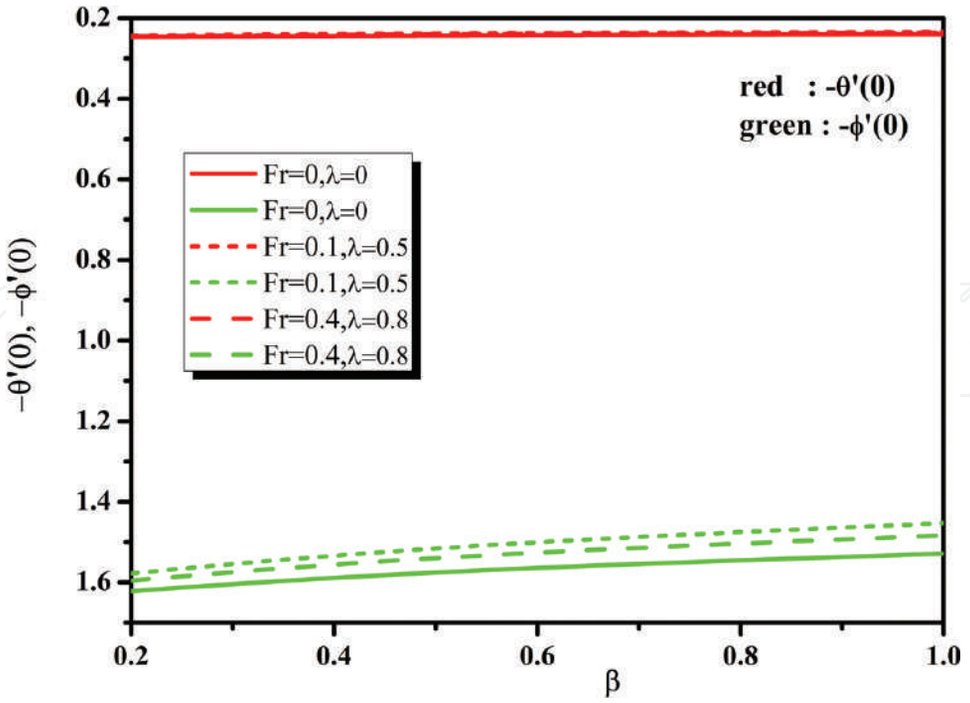

Figure 15. Variation of $-\theta'(0)$ and $-\phi'(0)$ with β for different values of Fr, λ.

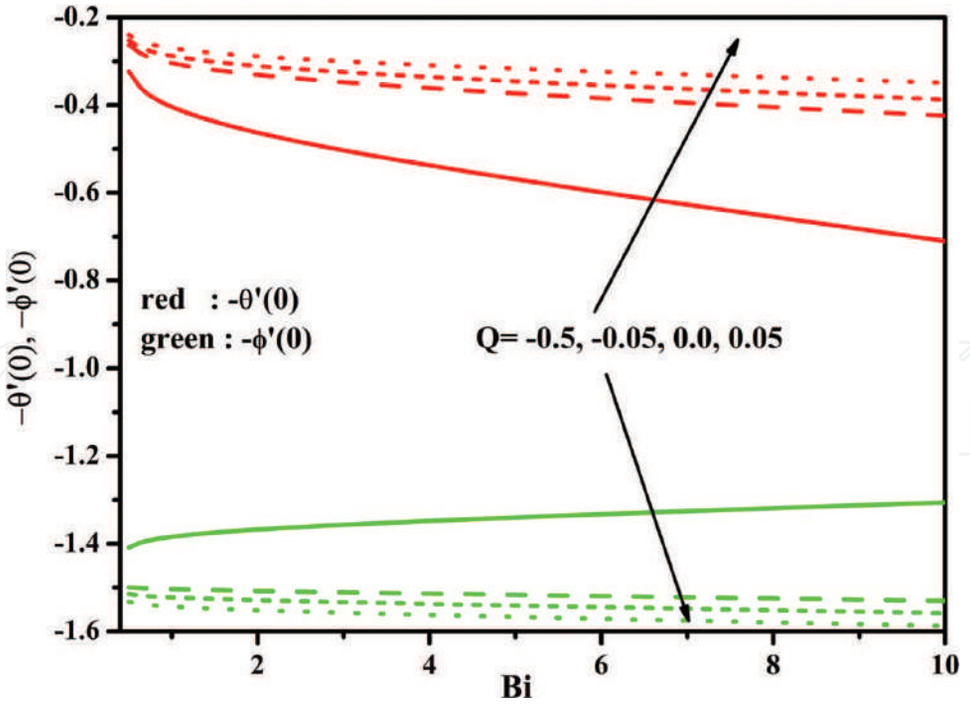

Figure 16. Variation of $-\theta'(0)$ and $-\phi'(0)$ with Bi for different values of Q.

http://dx.doi.org/10.5772/intechopen.74170

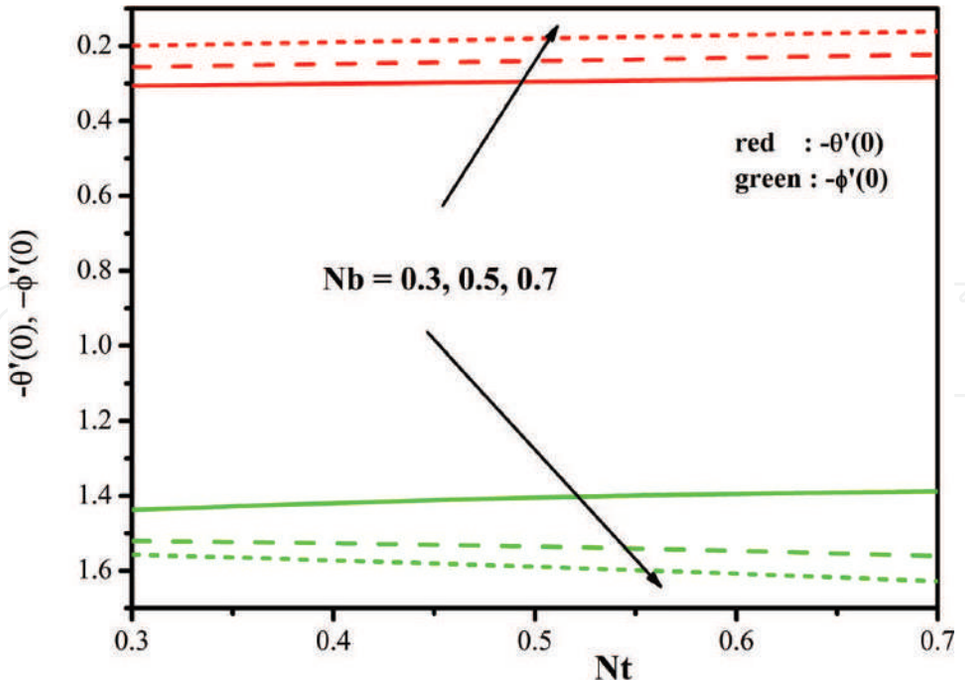

Figure 17. Variation of $-\theta'(0)$ and $-\phi'(0)$ with Nt for different values of Nb.

$\alpha = 1$, sheet will extended along the two bearings with a similar proportion (axisymmetric case), and third and last case identify with extending proportion parameter α other than 0 or 1; at that point, the flow conduct along both directions will be extraordinary.

Attributes of Forchheimer parameter (Fr) on $f'(\varsigma)$, $g'(\varsigma)$ is plotted in **Figure 3**. Obviously, $f'(\varsigma)$, $g'(\varsigma)$ is a diminishing capacity of Fr. **Figure 4** features the impact of Fr on $\theta(\varsigma)$, $\phi(\varsigma)$. Of course $\theta(\varsigma)$, $\phi(\varsigma)$ and related thickness of boundary layer are higher when Fr increments. **Figure 5** illustrates the varieties in $f'(\varsigma)$, $g'(\varsigma)$ for particular estimations of λ. Both $f'(\varsigma)$, $g'(\varsigma)$ and related layer thickness decay for larger λ. Physically, nearness of permeable media is to upgrade the protection from smooth movement which makes decay in fluid speed and thickness of energy boundary layer. **Figure 6** depicts the impact of λ on $\theta(\varsigma)$, $\phi(\varsigma)$. It is discovered that bigger λ causes an addition in $\theta(\varsigma)$, $\phi(\varsigma)$.

Figure 7 showed the impacts of non-Newtonian Casson fluid parameter (β) on velocity profiles $f'(\varsigma)$, $g'(\varsigma)$. It is seen that with the influence of β infers an abatement in the yield worry of the Casson fluid. This successfully encourages flow of the fluid, i.e., quickens the boundary layer flow near the extending surface, as appeared in **Figure 7**. In addition, it is found that with substantial estimations of β, the fluid is nearer to the Newtonian fluid. Truth be told, expanding estimations of the Casson fluid parameter β upgrade both temperature and nanoparticle division which is shown in **Figure 8**.

The variety in dimensionless temperature profile $\theta(\varsigma)$ with expanding estimations of generalized Prandtl number Pr is appeared through **Figure 9**. The temperature profile diminishes

with an expansion in the estimations of Prandtl number Pr, as Prandtl number is the proportion of energy diffusivity to thermal diffusivity. So, an expanding estimation of Prandtl number Pr infers a moderate rate of thermal dissemination which thus lessens the thermal boundary layer thickness. It can be directly seen that Prandtl number has more noticeable impact on Newtonian liquid when contrasted with non-Newtonian liquid.

Figure 10 displays the temperature $\theta(\varsigma)$ and the nanoparticle division $\phi(\varsigma)$ for variable estimations of Brownian movement *Nb*. The fluid velocity is found to increment with expanding *Nb*, while in nanoparticle fraction decreases as *Nb* expansion which consequently improves the nanoparticle's concentration at the sheet. This might be because of the way the Brownian movement parameter diminishes the mass exchange of a nanofluid. The diagram of thermophoresis parameter *Nt* on the temperature $\theta(\varsigma)$ and the nanoparticle part $\phi(\varsigma)$ profiles is portrayed in **Figure 11**. From these plots, it is seen that the impact of expanding estimations of *Nt* is to build the temperature and nanoparticle fraction.

Figure 12 shows the impact of Lewis number *Le* on temperature $\theta(\varsigma)$ and the nanoparticle portion $\phi(\varsigma)$ profiles. It is take note of that the temperature of the liquid increments however nanoparticle portion of the fluid diminishes with increment in *Le*. Physically truth that the bigger estimations of Lewis number makes the mass diffusivity littler, subsequently it diminishes the fixation field. The impacts of heat source/sink parameter *Q* can be found in **Figure 13**. For $Q > 0$ (heat source), it can be seen that the thermal boundary layer produces the vitality, and this causes the temperature in the thermal boundary layer increments with increment in *Q*. Though $Q < 0$ (heat sink) prompts diminish in the thermal boundary layer. $Q = 0$ speaks to the nonattendance of heat source/sink.

Impacts of the Biot number (*Bi*) on temperature are shown in **Figure 14**. Physically, the Biot number is communicated as the convection at the surface of the body to the conduction inside the surface of the body. At the point when thermal angle is connected at first glance, the proportion representing the temperature inside a body fluctuates significantly, while the body heats or cools over a period. Regularly, for uniform temperature field inside the surface, we consider $Bi << 1$. In any case, $Bi >> 1$ portrays that temperature field inside the surface is not uniform. In **Figure 14**, we have examined the impacts of Biot number *Bi* on the temperature and nanoparticle portion profiles in two ways. The first one is the situation.

when $Bi < 1$. It is seen from **Figure 14** that for the littlest estimations of the Biot number $Bi < 1$, the variety of temperature inside the body is slight and can sensibly be approximated as being uniform. While in the second case, $Bi > 1$ delineates that the temperature inside the body is not performing a uniform conduct (see **Figure 14**).

The impact of physical parameter on nearby Nusselt $-\theta'(0)$ and Sherwood number $-\phi'(0)$ is displayed in **Figure 15**. We can see through **Figure 15** that non-Darcy-Forchheimer connection creates the low heat and mass at the divider when contrasted with the Darcy-Forchheimer connection. Thus, it is seen with an expansion of the two reasons for speeding up in the λ and Fr. From **Figure 16**, the expanding estimations of the heat source/sink parameter (Q) improve the local Nusselt number $-\theta'(0)$ and decrease the local Sherwood number $-\phi'(0)$ with Bi . A similar conduct is likewise found for the variety in *Nt* and *Nb* which is portrayed in **Figure 17**.

http://dx.doi.org/10.5772/intechopen.74170

4. Conclusions

Three-dimensional flow of Casson nanoliquid within the sight of Darcy-Forchheimer connection, uniform warmth source/sink, and convective type boundary condition is considered. Numerical plan prompts the arrangements of physical marvel. From this investigation, we analyzed that the expanding Casson parameter compares to bring down velocity and higher temperature fields. The nearness of Fr and λ caused a lessening in velocity and increasing speed on temperature and nanoparticle portion. The bigger Biot number improved the temperature and nanoparticle division. Additionally, for vast estimations of Biot number, there are no noteworthy changes in $-\theta'(0)$ and $-\phi'(0)$, which are available in **Table 3**. In heat exchange issues, heat sink parameter controls the relative thickening of the force and the thermal boundary layers.

Bi	$-\theta'(0)$	$-\phi'(0)$
0.1	0.084997	1.521377
0.5	0.239615	1.532624
2	0.324388	1.568759
5	0.343057	1.582440
10	0.349174	1.587619
50	0.353999	1.591990
100	0.354597	1.592550
500	0.355075	1.593001
1000	0.355134	1.593057
5000	0.355182	1.593102
10,000	0.355188	1.593108
100,000	0.355193	1.593113
1,000,000	0.355194	1.593113
5,000,000	0.355194	1.593114

Table 3. Computational values of local Nusselt number and local Sherwood number for several values of *Bi*.

Author details

Gosikere Kenchappa Ramesh

Address all correspondence to: gkrmaths@gmail.com

Department of Mathematics, School of Engineering, Presidency University, Bengaluru, Karnataka, India

References

[1] Crane LJ. Flow past a stretching plate. Zeitschrift für angewandte Mathematik und Physik. 1970;**21**(4):645-647. DOI. org/10.1007/BF01587695

[2] Grubka LG, Bobba KM. Heat transfer characteristics of a continuous stretching surface with variable temperature. Journal of Heat Transfer. 1985;**107**(1):248-250. DOI: 10.1115/1.3247387

[3] Ali ME. Heat transfer characteristics of a continuous stretching surface. Heat and Mass Transfer. 1994;**29**(4);227-234. DOI.org/10.1007/BF01539754

[4] Gupta PS, Gupta AS. Heat and mass transfer on a stretching sheet with suction or blowing. Canadian Journal of Chemical Engineering. 1977;**55**:744746. DOI: 10.1002/cjce.5450550619

[5] Gireesha BJ, Ramesh GK, Subhas Abel M, Bagewadi CS. Boundary layer flow and heat transfer of a dusty fluid flow over a stretching sheet with non-uniform heat source/sink. International Journal of Multiphase Flow. 2011;**37**(8):977-982. DOI.org/10.1016/J.Ijmultiphaseflow.2011.03.014

[6] Ramesh GK, Gireesha BJ. Flow over a stretching sheet in a dusty fluid with radiation effect. ASME Journal of Heat transfer. 2013;**135**(10):102702(1-6). DOI: 10.1115/1.4024587

[7] Bataller RC. Radiation effects for the Blasius and Sakiadis flows with a convective surface boundary condition. Applied Mathematics and Computation. 2008;**206**:832-840. DOI.ORG/10.1016/J.AMC.2008.10.001

[8] Gorla RSR, Sidawi I. Free convection on a vertical stretching surface with suction and blowing. Applied Science Research. 1994;**52**:247-257. DOI.org/10.1007/BF00853952

[9] Ochoa MV. Analysis of drilling fluid rhelogy and tool joint effects to reduce errors in hydraulics calculations [thesis]. Texas A&M University; 2006

[10] Nadeem S, Rizwan Ul Haq, Lee C. MHD flow of a Casson fluid over an exponentially shrinking sheet. Scientia Iranica B. 2012;**19**(6):1550-1553. DOI.ORG/10.1016/J.SCIENT.2012.10.021

[11] Mukhopadhyay S. Casson fluid flow and heat transfer over a nonlinearly stretching. Chinese Physics B. 2013;**22**(7):074701. DOI.ORG/10.1088/1674-1056/22/7/074701

[12] Hayat T, Shehzad SA, Alsaedi A, Alhothuali MS. Mixed convection stagnation point flow of casson fluid with convective boundary conditions. Chinese Physical Letter. 2012;**29**(11);114704. DOI.org/10.1088/0256-307x/29/11/114704

[13] Ramesh GK, Ganesh Kumar K, Shehzad SA, Gireesha BJ. Enhancement of radiation on hydromagnetic Casson fluid flow towards a stretched cylinder with suspension of liquid-particles. Canadian Journal of Physics. 2018;**96**(1);18-24. DOI.ORG/10.1139/CJP-2017-0307

[14] Maity S, Singh SK, Kumar AV. Unsteady three dimensional flow of Casson liquid film over a porous stretching sheet in the presence of uniform transverse magnetic field and suction/injection. Journal of Magnetism and Magnetic Material. 2016;**419**:292-300. DOI. ORG/10.1016/J.JMMM.2016.06.004

[15] Nadeem S, Haq RU, Akbar NS, Khan ZH. MHD three-dimensional Casson fluid flow past a porous linearly stretching sheet. Alexandria Engineering Journal. 2013;**52**:577-582. DOI. ORG/10.1016/J.AEJ.2013.08.005

[16] Ahmad K, Nazar R. Magnetohydrodynamic three dimensional flow and heat transfer over a stretching surface in a viscoelastic fluid. Journal of Science and Technology. 2011; **3**(1):33-46

[17] Ramesh GK, Gireesha BJ, Shehzad SA, Abbasi FM. Analysis of heat transfer phenomenon in magnetohydrodynamic Casson fluid flow through Cattaneo-Christov heat diffusion theory. Communications in Theoretical Physics. 2017;**68**:91-95. DOI.ORG/10.1088/ 0253-6102/68/1/91

[18] Mustafa M, Hayat T, Pop I, Aziz A. Unsteady boundary layer flow of a Casson fluid due to an impulsively started moving flat plate. Heat Transfer-Asian Research. 2011;**40**(6): 563-576. DOI: 10.1002/htj.20358

[19] Buongiorno J. Convective transport in nanofluids. ASME Journal of Heat transfer. 2006; **128**:240-250. DOI: 10.1115/1.2150834

[20] Ahn HS, Kim MH. A review on critical heat flux enhancement with nanofluids and surface modification. Journal of Heat Transfer. 2012;**134**:024001. DOI: 10.1115/1.4005065

[21] Makinde OD, Aziz A. Boundary layer flow of a nanofluid past a stretching sheet with a convective boundary condition. International Journal of Thermal Science. 2011;**50**: 1326-1332. DOI.ORG/10.1016/J.IJTHERMALSCI.2011.02.019

[22] Hsiao KL. Nanofluid flow with multimedia physical features for conjugate mixed convection and radiation. Computers and Fluids. 2014;**104**:1-8. DOI.ORG/10.1016/J. COMPFLUID.2014.08.001

[23] Kuznetsov AV, Nield DA. Natural convective boundary layer flow of a nanofluid past a vertical plate: A revised model. International Journal of Thermal Science. 2014;**77**: 126-129. DOI.ORG/10.1016/J.IJTHERMALSCI.2013.10.007

[24] Hayat T, Muhammad T, Alsaedi A, Alhuthali MS. Magnetohydrodynamic three dimensional flow of viscoelastic nanofluid in the presence of nonlinear thermal radiation. Journal of Magnetism and Magnetic Materials. 2015;**385**:222-229. DOI.ORG/10.1016/J. JMMM.2015.02.046

[25] Ramesh GK, Roopa GS, Gireesha BJ, Shehzad SA, Abbasi FM. An electro-magnetohydrodynamic flow Maxwell nanoliquid past a Riga plate: A numerical study. Journal of the Brazilian Society of Mechanical Sciences and Engineering. 2017;**39**(11):4547-4554. DOI.org/10.1007/s40430-017-0900-z

[26] Ramesh GK, Prasannakumara BC, Gireesha BJ, Shehzad SA, Abbasi FM. Three dimensional flow of Maxwell nanofluid past a bidirectional porous stretching surface with thermal radiation. Thermal Science and Engineering Progress. 2017;**1**:6-14. DOI.ORG/10.1016/J.TSEP.2017.02.006

[27] Ramesh GK, Gireesha BJ. Influence of heat source/sink on a Maxwell fluid over a stretching surface with convective boundary condition in the presence of nanoparticles. Ain Shams Engineering Journal. 2014;**5**:991-998. DOI.ORG/10.1016/J.ASEJ.2014.04.003

[28] Forchheimer P. Wasserbewegung durch boden. Zeitschrift des Vereins deutscher Ingenieure. 1901;**45**:1782-1788

[29] Muskat M. The Flow of Homogeneous Fluids Through Porous Media. New York: McGraw Hill; 1937

[30] Pal D, Mondal H. Hydromagnetic convective diffusion of species in Darcy-Forchheimer porous medium with non-uniform heat source/sink and variable viscosity. International Communication in Heat and Mass Transfer. 2012;**39**:913-917. DOI.ORG/10.1016/J.ICHEATMASSTRANSFER.2012.05.012

[31] Hayat T, Muhammad T, Al-Mezal S, Liao SJ. Darcy-Forchheimer flow with variable thermal conductivity and Cattaneo-Christov heat flux. International Journal of Numerical Methods for Heat and Fluid Flow. 2016;**26**:2355-2369. DOI.ORG/10.1108/HFF-08-2015-0333

[32] Vishnu Ganesh N, Abdul Hakeem AK, Ganga B. Darcy–Forchheimer flow of hydromagnetic nanofluid over a stretching/shrinking sheet in a thermally stratified porous medium with second order slip, viscous and Ohmic dissipations effects. Ain Shams Engineering Journal. 2016. DOI.ORG/10.1016/J.ASEJ.2016.04.019 (In press)

[33] AdilSadiq M, Hayat T. Darcy–Forchheimer flow of magneto Maxwell liquid bounded by convectively heated sheet. Results in Physics. 2016;**6**:884-890. DOI.ORG/10.1016/J.RINP.2016.10.019

[34] Ishak A, Nazar R, Pop I. Magnetohydrodynamic (MHD) flow and heat transfer due to a stretching cylinder. Energy Conversion and Management. 2008;**49**:3265-3269. DOI.ORG/10.1016/J.ENCONMAN.2007.11.013

[35] Pal D, Mondal H. Influence of chemical reaction and thermal radiation on mixed convection heat and mass transfer over a stretching sheet in Darcian porous medium with Soret and Dufour effects. Energy Conversion and Management. 2012;**62**:102-108. DOI.ORG/10.1016/J.ENCONMAN.2012.03.017